A posteriori tests of subgrid-scale models in an isothermal turbulent channel flow

Dorian Dupuy, Adrien Toutant, Françoise Bataille

A posteriori tests of subgrid-scale models in an isothermal turbulent channel flow

Dorian Dupuy[1], Adrien Toutant*[1], and Françoise Bataille[1]

[1]*PROMES CNRS, Université de Perpignan Via Domitia, Rambla de la thermodynamique, Tecnosud, 66100 Perpignan, France*

(Published version: Physics of Fluids 31, 045105 (2019); https://doi.org/10.1063/1.5091829)

Abstract

This paper studies the large-eddy simulation (LES) of isothermal turbulent channel flows. We investigate zero-equation algebraic models without wall function or wall model: functional models, structural models and mixed models. In addition to models from the literature, new models are proposed and their relevance is examined. Dynamic versions of each type of model are also analysed. The performance of the subgrid-scale models is assessed using the same finite difference numerical method and physical configuration. The friction Reynolds number of the simulations is 180. Three different mesh resolutions are used. The predictions of large-eddy simulations are compared to a direct numerical simulation filtered at the resolution of the LES meshes. The results are more accurate than a simulation without model. The predictions of functional eddy-viscosity models can be improved using constant-parameter or dynamic tensorial methods.

1 Introduction

This paper addresses the large-eddy simulation (LES) of an isothermal turbulent channel flow at low Mach number. The large-eddy simulation of a turbulent channel flow is an important problem as it is one of the key canonical flows to understand wall-bounded turbulence. A large-eddy simulation only resolves the large-scale motions of turbulence, generally represented using a low-pass filter. This approach is more practical than direct numerical simulation (DNS), in which all scales of turbulence must be resolved. However, the evolution equations of the filtered variables cannot be inferred from the flow governing equations because the filter does not, in general, commute with multiplication. We consider the large-eddy simulation of the incompressible Navier–Stokes equations for a Newtonian fluid using a filter ($\overline{\cdot}$):

$$\frac{\partial \overline{U}_j}{\partial x_j} = 0, \tag{1}$$

$$\frac{\partial \overline{U}_i}{\partial t} = -\frac{\partial \left(\overline{U}_j \overline{U}_i + \tau_{ij}\right)}{\partial x_j} - \frac{1}{\rho}\frac{\partial \overline{P}}{\partial x_i} + \nu \frac{\partial^2 \overline{U}_i}{\partial x_j \partial x_i}, \tag{2}$$

with ρ the density, ν the kinematic viscosity, t the time, P the mechanical pressure, U_i the i-th component of velocity and x_i the Cartesian coordinate in i-th direction. The momentum convection subgrid term or subgrid-scale tensor is defined as $\tau_{ij} = \overline{U_j U_i} - \overline{U}_j \overline{U}_i$. To close

*Corresponding author : adrien.toutant@univ-perp.fr

the system of equations, the subgrid-scale tensor must be modelled using an algorithm computable in a large-eddy simulation. The addition of the subgrid-scale model should not violate the symmetry properties of Navier–Stokes equations [70, 52, 56]. In wall-bounded flows, the subgrid-scale model should be able to preserve the driving mechanisms of turbulence near the walls [32, 42, 33]. The consistency of the asymptotic near-wall behaviour of the model with the exact subgrid term is also considered very important [50, 51]. A review of the physical constraints that the subgrid-scale subgrid-scale model should satisfy is given in Silvis *et al.* [65]. Besides, for an application of these methods to another interesting problem, see references [86, 87].

The modelling of the subgrid-scale tensor has received a lot of attention from the literature. Algebraic or zero-equation models assume that the small scales are universal and can be expressed as functions of the resolved flow variables, as opposed to models requiring the resolution of one or more additional transport equations to compute the subgrid-scale model [60, 41]. The models can be classified into structural and functional models [60]. Functional models, also called eddy-viscosity models, make the fundamental hypothesis that the effect of subgrid scales is analogous to viscous diffusion [11], hence strictly dissipative. The popularity of this class of model is attributed to its robustness and low computational complexity [60, 75]. Structural models approximate the effect of the filter without assumptions on the physical nature of the effect of the subgrid term. A review is given by Lu and Rutland [41]. In the literature, numerous functional and structural models have been proposed and investigated in plane channel flows at low or moderate friction Reynolds numbers: the Smagorinsky and dynamic Smagorinsky models [26, 78, 34, 28, 6, 15, 35, 59, 53, 57, 75, 58, 84, 31], the approximate deconvolution model [71, 88], the rational model [26], the tensorial anisotropic model [1, 15, 2], the Kobayashi model [34], the Vreman and dynamic Vreman models [78, 59, 35, 75, 30, 84, 65, 31], the Sigma and dynamic Sigma models [6, 57, 35, 31], the QR and anisotropic minimum-dissipation (AMD) models [77, 58], the volumetric strain-stretching (VSS) model and dynamic VSS models [59, 84, 31], the anisotropy-resolving model [53], S3PQR models [75], the modulated gradient model [23], the vortex-stretching model [65], scale-adaptive models [84] and mixed and dynamic mixed models [46, 1, 35]. Note also that large-eddy simulation can be combined with Reynolds-averaged Navier–Stokes modelling, as in detached-eddy simulation [68, 74, 72, 69], in constrained large-eddy simulation [13, 29, 36] or in the linear unified model [24, 45, 44]. A systematic inspection of the subgrid-scale models would be useful for the selection of the subgrid-scale model for a particular simulation as well as for future subgrid-scale modelling developments.

This paper investigates a posteriori the modelling of the subgrid-scale tensor in an isothermal turbulent channel flow at a friction Reynolds number of 180. We will focus on the effect of the models on the turbulence statistics. To assess the performance of the large-eddy simulations, the results are compared to a direct numerical simulation filtered at the resolution of the large-eddy simulations. This allows the direct comparison of the results of the large-eddy simulations and of the direct numerical simulations. The analysis is based on the LES formalism introduced by Leonard [39]. In this paradigm, the large-eddy simulation aims to provide resolved fields whose statistics correspond to the statistics of a filtered direct numerical simulation. Note that the comparison with filtered direct numerical simulation is not systematically carried out in the literature since other approaches are possible [55]. For practical applications, the knowledge of the filtered variables may not be sufficient as nonfiltered variables are more relevant. This implies that a reconstruction of the nonfiltered fields from the results of the large-eddy simulation is required. By comparing large-eddy simulations to filtered DNS data, we separate the subgrid-scale modelling

from the reconstruction procedure, which may use a different model and can only address the deviatoric part of the Reynolds stresses for traceless or partially traceless models [82]. We address several functional and structural models from the literature using a common numerical method and physical configuration. In addition, tensorial eddy-viscosity models are proposed and investigated in order to explore the relevance of the eddy-viscosity assumption for each component of the subgrid term and account for the anisotropy of the flow. Mixed models combining structural and functional or tensorial models and dynamic versions of these models are also considered. The large-eddy simulations are carried out on three different meshes to provide an indication of the robustness of the models to variations of the grid resolution.

We give the subgrid-scale models investigated in section 2. The channel flow configuration and the numerical method are presented in section 3. The results are discussed in section 4.

2 Subgrid-scale models

Subgrid-scale models express the subgrid-scale tensor as a function of variables resolved in the large-eddy simulation:

$$\tau_{ij} \approx \tau_{ij}^{\mathrm{mod}}(\overline{\boldsymbol{U}}, \overline{\boldsymbol{\Delta}}), \tag{3}$$

where the function $\tau_{ij}^{\mathrm{mod}}(\boldsymbol{U}, \overline{\boldsymbol{\Delta}})$ depends on the model. We investigate zero-equation algebraic models without wall function or wall model. This includes functional models, structural models, tensorial models and tensorial mixed models. Dynamic versions of each type of modelling are also considered.

2.1 Constant-parameter models

Using functional eddy-viscosity models, the subgrid-scale tensor is modelled by analogy with molecular diffusion,

$$\tau_{ij}^{\mathrm{mod}}(\boldsymbol{U}, \overline{\boldsymbol{\Delta}}) = -2\nu_e^{\mathrm{mod}}(\boldsymbol{g}, \overline{\boldsymbol{\Delta}})S_{ij}, \tag{4}$$

with $S_{ij} = \frac{1}{2}\left(g_{ij} + g_{ji}\right)$ the rate of deformation tensor and $\boldsymbol{g}$ the velocity gradient, defined by $g_{ij} = \partial_j U_i$. The expression of the eddy viscosity depends on the model used. The eddy-viscosity models investigated are:

Smagorinsky model [67]:

$$\nu_e^{\mathrm{Smag.}}(\boldsymbol{g}, \overline{\boldsymbol{\Delta}}) = \left(C^{\mathrm{Smag.}}\overline{\Delta}\right)^2 |\boldsymbol{S}|, \tag{5}$$

Wall-adapting local eddy-viscosity (WALE) model [50]:

$$\nu_e^{\mathrm{WALE}}(\boldsymbol{g}, \overline{\boldsymbol{\Delta}}) = \left(C^{\mathrm{WALE}}\overline{\Delta}\right)^2 \frac{\left(\mathcal{S}_{ij}^d \mathcal{S}_{ij}^d\right)^{\frac{3}{2}}}{\left(S_{mn}S_{mn}\right)^{\frac{5}{2}} + \left(\mathcal{S}_{mn}^d \mathcal{S}_{mn}^d\right)^{\frac{5}{4}}}, \tag{6}$$

Sigma model [51]:

$$\nu_e^{\text{Sigma}}(\boldsymbol{g}, \overline{\boldsymbol{\Delta}}) = \left(C^{\text{Sigma}}\overline{\Delta}\right)^2 \frac{\sigma_3\left(\sigma_1-\sigma_2\right)\left(\sigma_2-\sigma_3\right)}{\sigma_1^2}, \tag{7}$$

Anisotropic minimum-dissipation (AMD) model [58]:

$$\nu_e^{\text{AMD}}(\boldsymbol{g}, \overline{\boldsymbol{\Delta}}) = C^{\text{AMD}} \frac{\max(0, -G_{ij}S_{ij})}{g_{mn}g_{mn}}, \tag{8}$$

Kobayashi model [34]:

$$\nu_e^{\text{Koba.}}(\boldsymbol{g}, \overline{\boldsymbol{\Delta}}) = C^{\text{Koba.}}\overline{\Delta}^2 \left|F_g\right|^{\frac{3}{2}} \left(1-F_g\right)|\boldsymbol{S}|, \tag{9}$$

where $|\boldsymbol{S}| = \sqrt{2S_{ij}S_{ij}}$ is a norm of $\boldsymbol{S}$, $\mathcal{S}_{ij}^d = \frac{1}{2}\left(g_{ik}g_{kj}+g_{jk}g_{ki}\right) - \frac{1}{3}g_{kp}g_{pk}\delta_{ij}$ the traceless symmetric part of the squared velocity gradient tensor, $\sigma_1 \geq \sigma_2 \geq \sigma_3$ the three singular values of $\boldsymbol{g}$, $G_{ij} = \overline{\Delta}_k^2 g_{ik}g_{jk}$ the gradient model, $\text{II}_G = \frac{1}{2}\left(\text{tr}^2\left(G\right) - \text{tr}\left(G^2\right)\right)$ its second invariant, $R_{ij} = \beta_i g_{jj}$ the volumetric strain-stretching, with $\beta = (S_{23}, S_{13}, S_{12})$, and $F_g = \left(\Omega_{ij}\Omega_{ij} - S_{ij}S_{ij}\right) / \left(\Omega_{mn}\Omega_{mn} + S_{mn}S_{mn}\right)$ the coherent structure function, with $\Omega_{ij} = \frac{1}{2}\left(g_{ij}-g_{ji}\right)$ the spin tensor or rate of rotation tensor.

Anisotropic eddy-viscosity models involve one length scale per direction instead of a single length scale. Anisotropic versions of the Smagorinsky, WALE, Sigma and Kobayashi models can be devised. The AMD model are already anisotropic. We define the Anisotropic Smagorinsky model [18] as,

$$\tau_{ij}^{\text{An.Smag.}}(\boldsymbol{U}, \overline{\boldsymbol{\Delta}}) = -2\nu_e^{\text{Smag.}}(\boldsymbol{g^a}, \overline{\boldsymbol{\Delta}})S_{ij}^a, \tag{10}$$

with $S_{ij}^a = \frac{1}{2}\left(g_{ij}^a + g_{ji}^a\right)$ the scaled rate of deformation tensor and $\boldsymbol{g^a}$ the scaled velocity gradient, defined by $g_{ij}^a = (\overline{\Delta}_j/\overline{\Delta})\partial_j U_i$.

Using the structural gradient model [39], the subgrid-scale tensor is modelled according to a Taylor series expansion of the filter,

$$\tau_{ij}^{\text{Grad.}}(\boldsymbol{U}, \overline{\boldsymbol{\Delta}}) = \tfrac{1}{12}C^{\text{Grad.}}G_{ij}(\boldsymbol{U}, \overline{\boldsymbol{\Delta}}) = \tfrac{1}{12}C^{\text{Grad.}}\overline{\Delta}_k^2 g_{ik}g_{jk}, \tag{11}$$

Using the structural scale-similarity model [5], the subgrid-scale tensor is modelled following the scale-similarity assumption,

$$\tau_{ij}^{\text{Simil.}}(\boldsymbol{U}, \overline{\boldsymbol{\Delta}}) = C^{\text{Simil.}}\left(\widehat{\overline{U_j}\overline{U_i}} - \widehat{\overline{U}}_j\,\widehat{\overline{U}}_i\right), \tag{12}$$

where $\widehat{\cdot}$ is a test filter explicitly computed in the large-eddy simulation. The Taylor series expansion of the filter $\widehat{\cdot}$ in (12) leads to

$$\tau_{ij}^{\text{Simil.}}(\boldsymbol{U}, \overline{\boldsymbol{\Delta}}) = \tfrac{1}{12}C^{\text{Simil.}}G_{ij}(\boldsymbol{U}, \widehat{\boldsymbol{\Delta}}) = \tfrac{1}{12}C^{\text{Simil.}}\widehat{\Delta}_k^2 g_{ik}g_{jk}. \tag{13}$$

This corresponds to the gradient model associated with the filter lengths $\widehat{\Delta}_k^2$ of the test filter.

Tensorial eddy-viscosity models can be constructed from any functional model. This aims to take into account the anisotropy of the flow by weighting of each component of the subgrid-scale model, following the premise that the relevance of the eddy-viscosity assumption is not the same for each component of the subgrid term. In general, we may

construct from any algebraic model $\tau_{ij}^{\mathrm{mod}}(\boldsymbol{U}, \overline{\boldsymbol{\Delta}})$, and second-order tensors $H_{ij}^{(k)}$ tensorial models $\tau_{ij}^{H^{(k)}\mathrm{mod}}(\boldsymbol{U}, \overline{\boldsymbol{\Delta}})$ of the form

$$\tau_{ij}^{H^{(k)}\mathrm{mod}}(\boldsymbol{U}, \overline{\boldsymbol{\Delta}}) = H_{ij}^{(k)} \tau_{ij}^{\mathrm{mod}}(\boldsymbol{U}, \overline{\boldsymbol{\Delta}}), \tag{14}$$

where no implicit summations over i and j are assumed. We define for this purpose the tensors $H_{ij}^{(1)} = [i \neq j]$, $H_{ij}^{(2)} = \left[\chi_{ij}^{xy}\right]$, $H_{ij}^{(3)} = \left[\neg\chi_{ij}^{yy}\right]$, $H_{ij}^{(4)} = \left[\chi_{ij}^{xy} \vee \chi_{ij}^{xz}\right]$, $H_{ij}^{(5)} = \left[\chi_{ij}^{xy} \vee \chi_{ij}^{yz}\right]$, $H_{ij}^{(6)} = [i = x \vee j = x]$ et $H_{ij}^{(7)} = \left[\chi_{ij}^{xx} \vee \chi_{ij}^{xy}\right]$, where $[\,\cdot\,]$ are Iverson brackets, evaluating to 1 if the proposition within bracket is satisfied and 0 otherwise, $\neg$ the logical negation (NOT), $\wedge$ the logical conjunction (AND), $\vee$ the logical disjunction (OR) and with the notation $\chi_{ij}^{ab} = (i = a \wedge j = b) \vee (i = b \wedge j = a)$. More explicitly, we have

$$H^{(1)} = \begin{pmatrix} 0 & 1 & 1 \\ 1 & 0 & 1 \\ 1 & 1 & 0 \end{pmatrix}, \tag{15}$$

$$H_{ij}^{(2)} = \begin{pmatrix} 0 & 1 & 0 \\ 1 & 0 & 0 \\ 0 & 0 & 0 \end{pmatrix}, \tag{16}$$

$$H_{ij}^{(3)} = \begin{pmatrix} 1 & 1 & 1 \\ 1 & 0 & 1 \\ 1 & 1 & 1 \end{pmatrix}, \tag{17}$$

$$H_{ij}^{(4)} = \begin{pmatrix} 0 & 1 & 1 \\ 1 & 0 & 0 \\ 1 & 0 & 0 \end{pmatrix}, \tag{18}$$

$$H_{ij}^{(5)} = \begin{pmatrix} 0 & 1 & 0 \\ 1 & 0 & 1 \\ 0 & 1 & 0 \end{pmatrix}, \tag{19}$$

$$H_{ij}^{(6)} = \begin{pmatrix} 1 & 1 & 1 \\ 1 & 0 & 0 \\ 1 & 0 & 0 \end{pmatrix}, \tag{20}$$

$$H_{ij}^{(7)} = \begin{pmatrix} 1 & 1 & 0 \\ 1 & 0 & 0 \\ 0 & 0 & 0 \end{pmatrix}. \tag{21}$$

Functional and structural models may also be combined to form mixed models. To be more general, we consider tensorial mixed models, which combine the two models with a different weighting for each component. This may be used to combine structural and functional models for each component or to model each component with either a functional or a structural model. Tensorial mixed models are constructed from two algebraic models $\tau_{ij}^{\mathrm{one}}(\boldsymbol{U}, \overline{\boldsymbol{\Delta}})$ and $\tau_{ij}^{\mathrm{two}}(\boldsymbol{U}, \overline{\boldsymbol{\Delta}})$, and two constant second-order tensors $H^{(k)}$ and $H^{(l)}$,

$$\begin{aligned} \tau_{ij}^{(1-H^{(k)})\mathrm{one}+H^{(l)}\mathrm{two}}(\overline{\boldsymbol{U}}, \overline{\boldsymbol{\Delta}}) = (1 - H_{ij}^{(k)}) \tau_{ij}^{\mathrm{one}}(\overline{\boldsymbol{U}}, \overline{\boldsymbol{\Delta}}) \\ + H_{ij}^{(l)} \tau_{ij}^{\mathrm{two}}(\overline{\boldsymbol{U}}, \overline{\boldsymbol{\Delta}}). \end{aligned} \tag{22}$$

where no implicit summations over i and j are assumed.

Unless stated otherwise, we implicitly use the model parameters $C^{\mathrm{Smag.}} = 0.10$, $C^{\mathrm{WALE}} = 0.55$, $C^{\mathrm{Sigma}} = 1.5$, $C^{\mathrm{AMD}} = 0.3$ and $C^{\mathrm{Koba.}} = 0.045$. We compute the filter length scale

using $\overline{\Delta} = (\overline{\Delta}_x \overline{\Delta}_y \overline{\Delta}_z)^{1/3}$ [14]. The reader may refer to Trias *et al.* [76] for a review of alternative definitions.

2.2 Dynamic models

For any constant-parameter algebraic subgrid-scale model, dynamic models may be constructed using the approach introduced by Germano *et al.* [22]. A new model $\tau_{ij}^{\mathrm{dyn,mod}}(\boldsymbol{U}, \overline{\boldsymbol{\Delta}})$, referred to as the dynamic version of the model, can be constructed from any algebraic model $\tau_{ij}^{\mathrm{mod}}(\boldsymbol{U}, \overline{\boldsymbol{\Delta}})$,

$$\tau_{ij}^{\mathrm{dyn,mod}}(\overline{\boldsymbol{U}}, \overline{\boldsymbol{\Delta}}) = C^{\mathrm{dyn}} \tau_{ij}^{\mathrm{mod}}(\overline{\boldsymbol{U}}, \overline{\boldsymbol{\Delta}}). \tag{23}$$

Following the approach of Lilly [40], the parameter C^{dyn} is computed to minimise the variance of the residual $E_{ij}(\overline{\boldsymbol{U}}, \overline{\boldsymbol{\Delta}}) = L_{ij}(\overline{\boldsymbol{U}}) - C^{\mathrm{dyn}} m_{ij}(\overline{\boldsymbol{U}}, \overline{\boldsymbol{\Delta}})$. This leads to

$$C^{\mathrm{dyn}} = \frac{\left\langle m_{ij}(\overline{\boldsymbol{U}}, \overline{\boldsymbol{\Delta}}) L_{ij}(\overline{\boldsymbol{U}}) \right\rangle}{\left\langle m_{mn}(\overline{\boldsymbol{U}}, \overline{\boldsymbol{\Delta}}) m_{mn}(\overline{\boldsymbol{U}}, \overline{\boldsymbol{\Delta}}) \right\rangle}. \tag{24}$$

$L_{ij}(\overline{\boldsymbol{U}}) = \widehat{\overline{U}_j \overline{U}_i} - \widehat{\overline{U}}_j \widehat{\overline{U}}_i$, with $m_{ij}(\overline{\boldsymbol{U}}, \overline{\boldsymbol{\Delta}}) = \tau_{ij}^{\mathrm{mod}}(\widehat{\overline{\boldsymbol{U}}}, \widehat{\overline{\boldsymbol{\Delta}}}) - \widehat{\tau_{ij}^{\mathrm{mod}}(\overline{\boldsymbol{U}}, \overline{\boldsymbol{\Delta}})}$ and where $(\widehat{\cdot})$ is a test filter. The value of $\widehat{\overline{\Delta}}$ is best approximated as $\widehat{\overline{\Delta}} = (\overline{\Delta}_i^2 + \widehat{\Delta}_i^2)^{1/2}$ for Gaussian and box filters [21, 80]. Tensorial dynamic methods can extend the dynamic procedure to the construction of models of the form

$$\tau_{ij}^{\mathrm{ten,dyn,mod}}(\overline{\boldsymbol{U}}, \overline{\boldsymbol{\Delta}}) = C_{ij}^{\mathrm{dyn}} \tau_{ij}^{\mathrm{mod}}(\overline{\boldsymbol{U}}, \overline{\boldsymbol{\Delta}}), \tag{25}$$

where no implicit summations over i and j are assumed. As in the (scalar) dynamic method, the tensorial parameter of the model is computed dynamically to minimise for all i and j the variance of the residual [1]. This leads to

$$C_{ij}^{\mathrm{dyn}} = \frac{\left\langle m_{ij}(\overline{\boldsymbol{U}}, \overline{\boldsymbol{\Delta}}) L_{ij}(\overline{\boldsymbol{U}}) \right\rangle}{\left\langle m_{ij}(\overline{\boldsymbol{U}}, \overline{\boldsymbol{\Delta}}) m_{ij}(\overline{\boldsymbol{U}}, \overline{\boldsymbol{\Delta}}) \right\rangle}, \tag{26}$$

where no implicit summations over i and j are assumed.

In addition, dynamic mixed models can be constructed using analogous procedures. The dynamic mixed model $\tau_{ij}^{\mathrm{dyn,one,two}}(\boldsymbol{U}, \overline{\boldsymbol{\Delta}})$ may be expressed from two algebraic models $\tau_{ij}^{\mathrm{one}}(\boldsymbol{U}, \overline{\boldsymbol{\Delta}})$ and $\tau_{ij}^{\mathrm{two}}(\boldsymbol{U}, \overline{\boldsymbol{\Delta}})$ as

$$\tau_{ij}^{\mathrm{dyn,one,two}}(\overline{\boldsymbol{U}}, \overline{\boldsymbol{\Delta}}) = C^{\mathrm{one}} \tau_{ij}^{\mathrm{one}}(\overline{\boldsymbol{U}}, \overline{\boldsymbol{\Delta}}) + C^{\mathrm{two}} \tau_{ij}^{\mathrm{two}}(\overline{\boldsymbol{U}}, \overline{\boldsymbol{\Delta}}). \tag{27}$$

Several methods have been suggested to compute the parameters C^{one} and C^{two}:

- Two-parameter dynamic mixed method: The parameters of the two models are computed dynamically to minimise the variance of the residual $E_{ij} = L_{ij} - C^{\mathrm{one}} m_{ij}^{\mathrm{one}} - C^{\mathrm{two}} m_{ij}^{\mathrm{two}}$ [62, 63, 25, 64]. This leads to

$$C^{\mathrm{two}} = \frac{\left\langle m_{ij}^{\mathrm{one}} m_{ij}^{\mathrm{one}} \right\rangle \left\langle L_{kl} m_{kl}^{\mathrm{two}} \right\rangle - \left\langle m_{ij}^{\mathrm{one}} m_{ij}^{\mathrm{two}} \right\rangle \left\langle m_{kl}^{\mathrm{one}} L_{kl} \right\rangle}{\left\langle m_{mn}^{\mathrm{one}} m_{mn}^{\mathrm{one}} \right\rangle \left\langle m_{pq}^{\mathrm{two}} m_{pq}^{\mathrm{two}} \right\rangle - \left\langle m_{mn}^{\mathrm{one}} m_{mn}^{\mathrm{two}} \right\rangle \left\langle m_{pq}^{\mathrm{one}} m_{pq}^{\mathrm{two}} \right\rangle}. \tag{28}$$

  with $m_{ij}^{\mathrm{one}}(\overline{\boldsymbol{U}}, \overline{\boldsymbol{\Delta}}) = \tau_{ij}^{\mathrm{one}}(\widehat{\overline{\boldsymbol{U}}}, \widehat{\overline{\boldsymbol{\Delta}}}) - \widehat{\tau_{ij}^{\mathrm{one}}(\overline{\boldsymbol{U}}, \overline{\boldsymbol{\Delta}})}$ and $m_{ij}^{\mathrm{two}}(\overline{\boldsymbol{U}}, \overline{\boldsymbol{\Delta}}) = \tau_{ij}^{\mathrm{two}}(\widehat{\overline{\boldsymbol{U}}}, \widehat{\overline{\boldsymbol{\Delta}}}) - \widehat{\tau_{ij}^{\mathrm{two}}(\overline{\boldsymbol{U}}, \overline{\boldsymbol{\Delta}})}$. The parameter C^{one} may be computed from the permutation of the exponents "one" and "two" in the above expression.

- One-parameter dynamic mixed method: The parameter of one of the two models is arbitrarily set, for instance C^{one}, then the parameter of the other model is computed dynamically to minimise the variance of the residual [85, 80]. This leads to

$$C^{\text{two}} = \frac{\left\langle m_{ij}^{\text{two}} \left(L_{ij} - C^{\text{one}} m_{ij}^{\text{one}} \right) \right\rangle}{\langle m_{mn}^{\text{two}} m_{mn}^{\text{two}} \rangle}. \tag{29}$$

  The parameter of the first model C^{one} may be set to a constant. Alternatively, it may be computed with the classical dynamic method, that is without taking into consideration the second model. This has been suggested in order to improve the two-parameter dynamic procedure [3, 46].

A generalisation of dynamic mixed models to an arbitrary number of parameters is given by Sagaut *et al.* [61].

The dynamic procedure may be extended to the construction of a model using tensorial parameters C_{ij}^{one} and C_{ij}^{two},

$$\tau_{ij}^{\text{dyn,one,two}}(\overline{\boldsymbol{U}}, \overline{\boldsymbol{\Delta}}) = C_{ij}^{\text{one}} \tau_{ij}^{\text{one}}(\overline{\boldsymbol{U}}, \overline{\boldsymbol{\Delta}}) + C_{ij}^{\text{two}} \tau_{ij}^{\text{two}}(\overline{\boldsymbol{U}}, \overline{\boldsymbol{\Delta}}), \tag{30}$$

where no implicit summations over i and j are assumed. The dynamic methods (28) and (29) can be extended to tensorial parameters:

- Tensorial two-parameter dynamic mixed method: As in the (scalar) two-parameter dynamic mixed method, the parameters of the two models are computed dynamically to minimise for all i and j the variance of the residual. This leads to

$$C_{ij}^{\text{two}} = \frac{\left\langle m_{ij}^{\text{one}} m_{ij}^{\text{one}} \right\rangle \left\langle L_{ij} m_{ij}^{\text{two}} \right\rangle - \left\langle m_{ij}^{\text{one}} m_{ij}^{\text{two}} \right\rangle \left\langle m_{ij}^{\text{one}} L_{ij} \right\rangle}{\left\langle m_{ij}^{\text{one}} m_{ij}^{\text{one}} \right\rangle \left\langle m_{ij}^{\text{two}} m_{ij}^{\text{two}} \right\rangle - \left\langle m_{ij}^{\text{one}} m_{ij}^{\text{two}} \right\rangle \left\langle m_{ij}^{\text{one}} m_{ij}^{\text{two}} \right\rangle}, \tag{31}$$

  where no implicit summations over i and j are assumed. The parameter C^{one} may be computed from the permutation of the exponents "one" and "two" in the above expression.

- Tensorial one-parameter dynamic mixed method: As in the (scalar) one-parameter dynamic mixed method, the parameters of one of the two models are arbitrarily set, the parameters of the other model being computed dynamically to minimise for all i and j the variance of the residual. This leads to

$$C_{ij}^{\text{two}} = \frac{\left\langle m_{ij}^{\text{two}} \left(L_{ij} - C^{\text{one}} m_{ij}^{\text{one}} \right) \right\rangle}{\left\langle m_{ij}^{\text{two}} m_{ij}^{\text{two}} \right\rangle}, \tag{32}$$

  where no implicit summations over i and j are assumed. The parameter of the first model C^{one} either be set to a constant or computed using the classical tensorial dynamic method.

For each dynamic procedure, the average $\langle \cdot \rangle$ can be computed as a plane average, that is over the homogeneous directions, or as a global average [54, 83, 37, 7, 66], that is over the volume of the channel. The parameter of plane-average dynamic procedures is a function of time and the wall-normal coordinate. The parameter of global-average dynamic procedures is a function of time.

Re_τ	Name	Number of grid points $N_x \times N_y \times N_z$	Dimension of the domain $L_x \times L_y \times L_z$	Cell sizes in wall units $\Delta_x^+; \Delta_y^+(0)$–$\Delta_y^+(h); \Delta_z^+$	Mesh dilatation parameter a
180	48B	$48 \times 50 \times 48$	$4\pi h \times 2h \times 2\pi h$	68 ; 0.50 – 25 ; 34	0.981
180	36C	$36 \times 40 \times 36$	$4\pi h \times 2h \times 2\pi h$	91 ; 2.0 – 22 ; 45	0.910
180	24C	$24 \times 28 \times 24$	$4\pi h \times 2h \times 2\pi h$	136 ; 2.0 – 35 ; 68	0.949
180	DNS	$384 \times 266 \times 384$	$4\pi h \times 2h \times 2\pi h$	5.8 ; 0.085 – 2.9 ; 2.9	0.971

Table 1 – Computational domain and grid spacing of the DNS mesh and the three LES meshes. The cell sizes in wall units are computed using the friction velocity of the direct numerical simulation.

3 Numerical study configuration

3.1 Channel flow configuration

We investigate the large-eddy simulation of a fully developed three-dimensional turbulent channel flow. The channel is periodic in the streamwise (x) and spanwise (z) directions and enclosed by two plane walls in the wall-normal direction (y). The flow is isothermal and incompressible. The mean friction Reynolds number is $Re_\tau = 180$. The domain size is $4\pi h \times 2h \times 2\pi h$. To analyse the results, we use a direct numerical simulation of the same channel presented in Dupuy *et al.* [17], and validated against the reference data of Moser *et al.* [48], Bolotnov *et al.* [10], Vreman and Kuerten [79] and Lee and Moser [38].

3.2 Numerical settings

The channel flow presented in section 3.1 is simulated using three meshes, referred to as "48B", "36C" and "24C". The meshes are rectilinear. The grid spacing is uniform in the homogeneous directions (x and z) and follows a hyperbolic tangent law in the wall-normal coordinate direction (y),

$$y_k = L_y \left(1 + \frac{1}{a} \tanh\left[\left(\frac{k-1}{N_y - 1} - 1\right) \tanh^{-1}(a)\right]\right), \tag{33}$$

with a the mesh dilatation parameter and N_y the number of grid points in the wall-normal direction. The domain size and grid spacing of the simulations are given in table 1. We use a finite difference method in a staggered grid system [47, 49] with a fourth-order centred momentum convection scheme, a second-order centred diffusion scheme and a third-order Runge–Kutta time scheme [81]. If present, the eddy viscosity is computed and discretised at the center of control volumes in the same way as molecular viscosity and the operators $\partial_j(\mu g_{ij})$ and $\partial_j(\mu g_{ji})$ are discretised directly using second-order centred schemes. The simulations are performed using the TrioCFD software [12]. This software has been used in many numerical simulations of fluid flows [73, 4, 19].

The direct numerical simulations use the same numerical method as the large-eddy simulations and have the same domain size.

3.3 Filtering process

In order to allow the direct comparison of the results of the large-eddy simulations and of the direct numerical simulations, we filter the instantaneous DNS data at the resolution of the LES meshes. We use a top-hat filter to perform this filtering. To carry out the box filter, we first interpolate the DNS data using a cubic spline then compute the filter from the interpolated data, as in [16, 18]. The cubic spline interpolation allows the computation of the filter with an arbitrary filter length and without mesh restrictions. The spline interpolation adds an additional filtering to the box filter. However, this additional filter is small compared to the box filter with the DNS mesh used and can be neglected.

Filtering is also required to compute the test filter involved in some subgrid-scale models. These filters are computed using other methods because the spline interpolation is too computationally expensive to be used in a large-eddy simulation. The test filter of dynamic methods, referred to as "filter A" is computed as an average over three cells in the three directions. This approximates a top-hat filter whose width is thrice as large as the LES mesh. The test filter of the scale-similarity model has been computed using the filter A and another filter. The second filter, referred to as "filter T", uses the Taylor series expansion of the box filter using the local cell size as the filter width.

4 Results and discussion

The large-eddy simulations are used to study the relevance of models for the subgrid-scale tensor. Before proceeding to the comparison of the subgrid-scale models, we briefly discuss the simulation of the channel without subgrid-scale model. To analyse the results, we use two types of scaling. With the wall scaling ($^+$), all quantities are scaled using a combination of the friction velocity U_τ and the kinematic viscosity ν, $y^+ = yU_\tau/\nu$ and $\boldsymbol{U}^+ = \boldsymbol{U}/U_\tau$. With the scaling ($^\circ$), all quantities are scaled using a combination of the channel half-height and the kinematic viscosity ν, $y^\circ = y/h$ and $\boldsymbol{U}^\circ = \boldsymbol{U}h/\nu$.

4.1 Simulation without subgrid-scale models

Simulations without subgrid-scale model are carried out with the meshes 24C, 36C and 48B. These simulations aim to provide reference data without any subgrid-scale modelling. Although no explicit subgrid-scale models are used, the approach differs from implicit large-eddy simulation, which is usually based on the use of the dissipative properties of specific numerical schemes to model the small-scale motions [60], as our numerical method is intended to cause minimal dissipation. The mass flow rate of the simulations is imposed using a control loop to adjust the streamwise volume force f. The targeted mass flow rate is the same as in the direct numerical simulations. Accordingly, the simulations have the same mass flow rate than the direct numerical simulations but predict a different wall shear stress. With the mesh 48B, the error on the friction velocity is 2%. Imposing a constant streamwise volume force would maintain the wall shear stress at the same level as the direct numerical simulations, but results in an error of 2% on the mass flow rate. The results of simulations with constant mass flow rate and constant streamwise volume force are compared in figure 1. The scaling of the profiles takes into account the differences of mass flow rate. Nevertheless, the two approaches are not completely equivalent because the Reynolds number differences between the two methods may induce low Reynolds number effects.

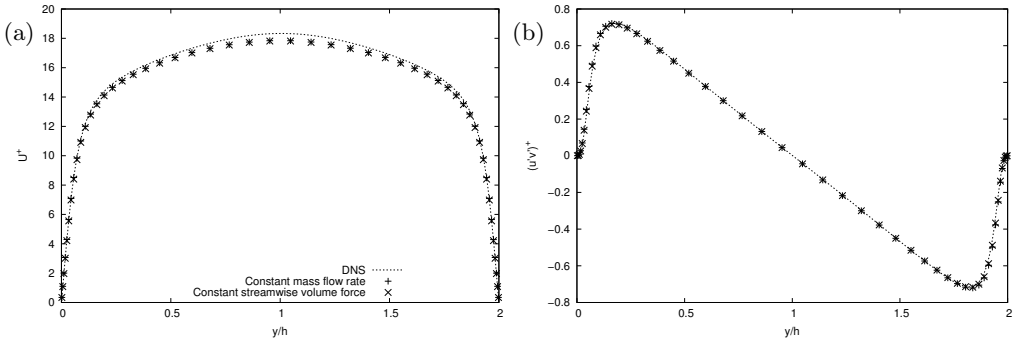

Figure 1 – Comparison of simulations with no subgrid-scale model with constant mass flow rate and constant streamwise volume force for the profiles of the mean streamwise velocity $\langle U_x \rangle$ (left) and the covariance of streamwise and wall-normal velocity $\langle u'_x u'_y \rangle$ (right) with the mesh 48B.

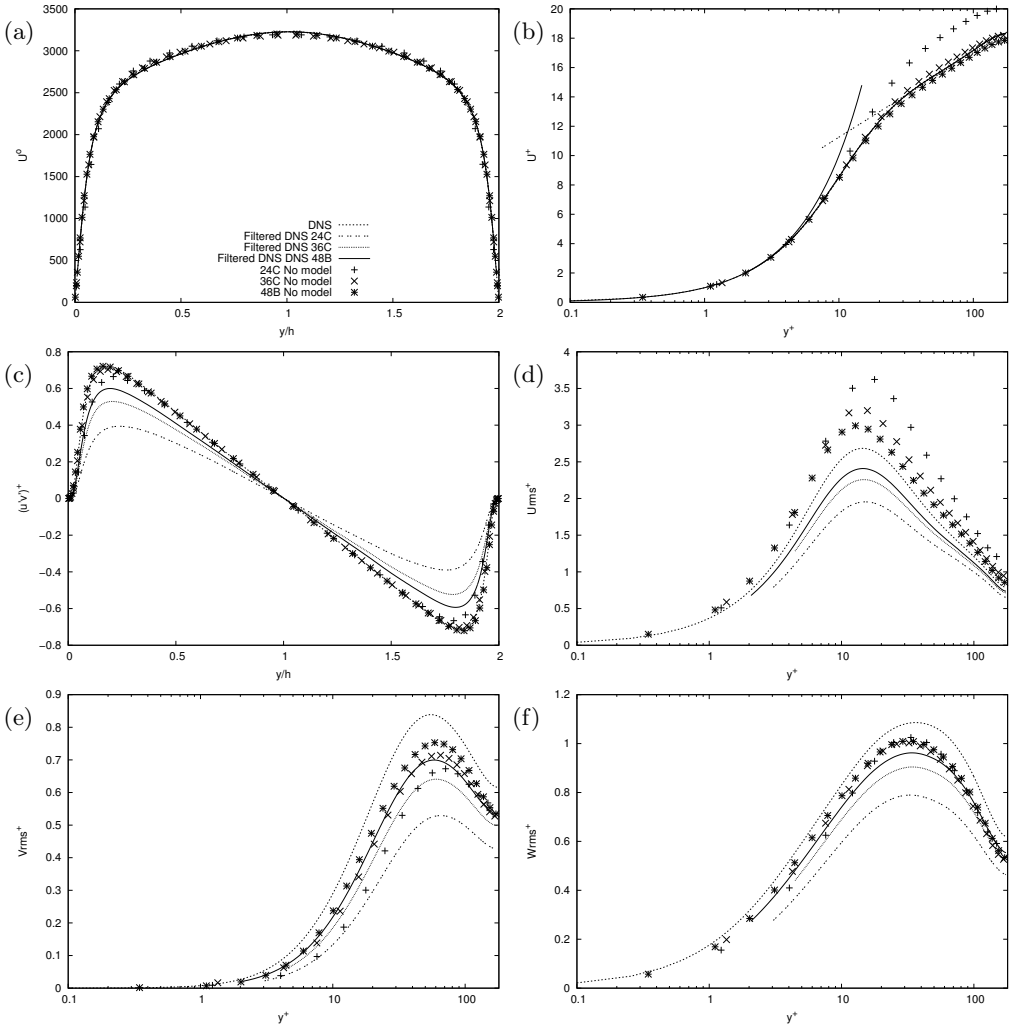

Figure 2 – Comparison of simulations with no subgrid-scale model with the meshes 24C, 36C and 48B for the profiles of the mean streamwise velocity $\langle U_x \rangle$ (a, b), the covariance of streamwise and wall-normal velocity $\langle u'_x u'_y \rangle$ (c), the standard deviation of streamwise velocity $\sqrt{\langle u'^2_x \rangle}$ (d), wall-normal velocity $\sqrt{\langle u'^2_y \rangle}$ (e) and spanwise velocity $\sqrt{\langle u'^2_z \rangle}$ (f).

The results of the simulations without subgrid-scale model with the meshes 24C, 36C and 48B are compared in figure 2. The profiles of the turbulence statistics are compared to direct numerical simulations filtered at the resolution of the simulation meshes. The mean nonfiltered and filtered streamwise velocity are almost identical, because the filtered field has sufficient spectral content [82]. Nevertheless, the simulation with the mesh 24C underestimates significantly the friction velocity, and thus the mean streamwise velocity near the wall. The mean streamwise velocity is without scaling satisfactory at the center of the channel for all simulations (figure 2).

The filtering of the DNS data decreases significantly the maximum value of the covariance of streamwise and wall-normal velocity and the standard deviation of velocity components. The decrease is larger for a larger filter width. The decrease ranges from around 10% with the mesh 48B to around 30% with the mesh 24C. However, the simulations without model lead with the three meshes to a similar covariance of streamwise and wall-normal velocity and standard deviation of spanwise velocity, while the standard deviation of streamwise velocity increases with mesh derefinement (figure 2). The interpretation of these results should take into account the effect of the classical scaling, as the underestimation of the wall shear stress in the coarser simulations offsets a slight decrease of the covariance of streamwise and wall-normal velocity and the standard deviation of spanwise velocity without scaling.

The error on the friction velocity is 9% with the mesh 24C, 6% with the mesh 36C and 2% with the mesh 48B. The relative accuracy of the wall shear stress with the mesh 48B is partly due to its non-monotonous convergence of the prediction with mesh refinement. As identified by Meyers and Sagaut [43], the non-monotonous convergence allows the existence of a grid-resolution line where the error on the wall shear stress is zero. The simulation of the channel with a finer $72 \times 68 \times 72$ mesh leads to an error of 4% for the wall shear stress. This is less accurate than with the mesh 48B, confirming that the mesh 48B is close to Meyers' no error line. Due to this non-monotonous convergence of the wall shear stress and the turbulence statistics, it is important to verify the robustness of the subgrid-scale models to a range of grid resolutions.

Thus, while the mean streamwise velocity is fairly well represented by the simulations without model, more complex turbulence statistics, such as the Reynolds stresses, are less accurate. In the following, we will study the simulation of the channel with subgrid-scale models, that is its large-eddy simulation, and examine whether the addition of a subgrid-scale model can improve these results. To study the modelling of the subgrid-scale tensor, we carry out large-eddy simulations with several functional models, structural models, tensorial models and tensorial mixed models.

4.2 Functional modelling

In this section, we investigate the functional modelling of the subgrid-scale tensor. The functional models investigated are the Smagorinsky, WALE, Sigma, AMD, Kobayashi and Anisotropic Smagorinsky models, as well as dynamic versions of these models. The results of large-eddy simulations with these models are compared in figure 3 with the mesh 48B. As consistently found in the literature [see e.g. 78], the Smagorinsky model does not perform well in shear flow and considerably deteriorates the profiles of the turbulence statistics. The Anisotropic Smagorinsky model improves significantly the predictions compared to the Smagorinsky model, providing similar results to the WALE, Sigma and AMD models. The WALE, Sigma, AMD, Kobayashi and Anisotropic Smagorinsky models underestimate the

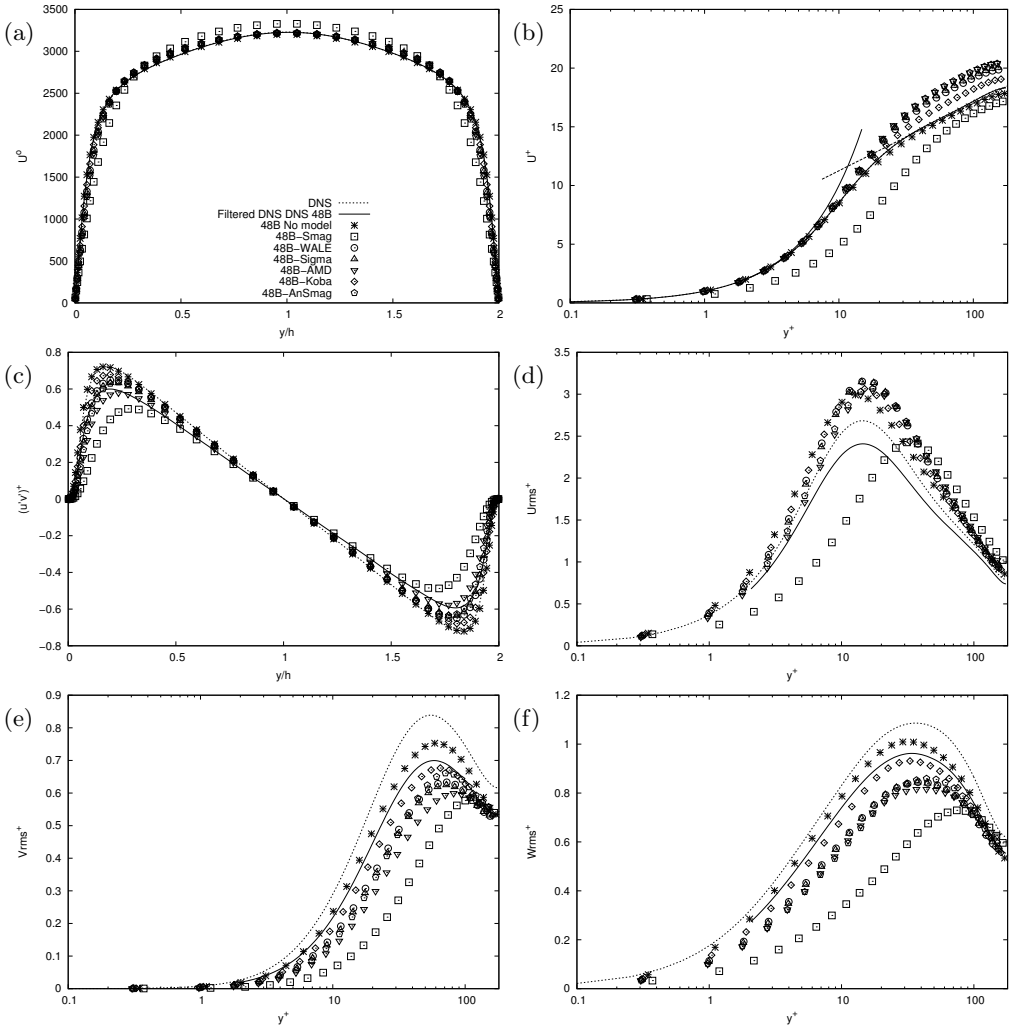

Figure 3 – Comparison of large-eddy simulations with the Smagorinsky, WALE, Sigma, AMD, Kobayashi and Anisotropic Smagorinsky models for the profiles of the mean streamwise velocity $\langle U_x \rangle$ (a, b), the covariance of streamwise and wall-normal velocity $\langle u'_x u'_y \rangle$ (c), the standard deviation of streamwise velocity $\sqrt{\langle u'^2_x \rangle}$ (d), wall-normal velocity $\sqrt{\langle u'^2_y \rangle}$ (e) and spanwise velocity $\sqrt{\langle u'^2_z \rangle}$ (f) with the mesh 48B.

wall shear stress, thus do not lead to a good representation of the scaled mean streamwise velocity. The additional dissipation provided by the model is able to decrease the maximum value of the standard deviation of wall-normal and spanwise velocity, but the standard deviation of streamwise velocity is increased further away from the filtered DNS profile. The no-model simulation yields a better prediction of the friction Reynolds number, the mean streamwise velocity and the standard deviation of velocity components than the large-eddy simulations with functional models. The points discussed above are also valid for the meshes 24C and 36C. The larger filter widths amplify the reduction of the standard deviation of wall-normal and spanwise velocity following approximately the same behaviour as the filtered direct numerical simulation (figure 4). On the other hand, the standard deviation of streamwise velocity is even with the 24C mesh not reduced compared to the no-model simulation, further enhancing the discrepancy with the filtered direct numerical simulation. The predictions of the large-eddy simulations depend on the amplitude of the subgrid-scale viscosity. In our simulations, a lower subgrid-scale viscosity is obtained with

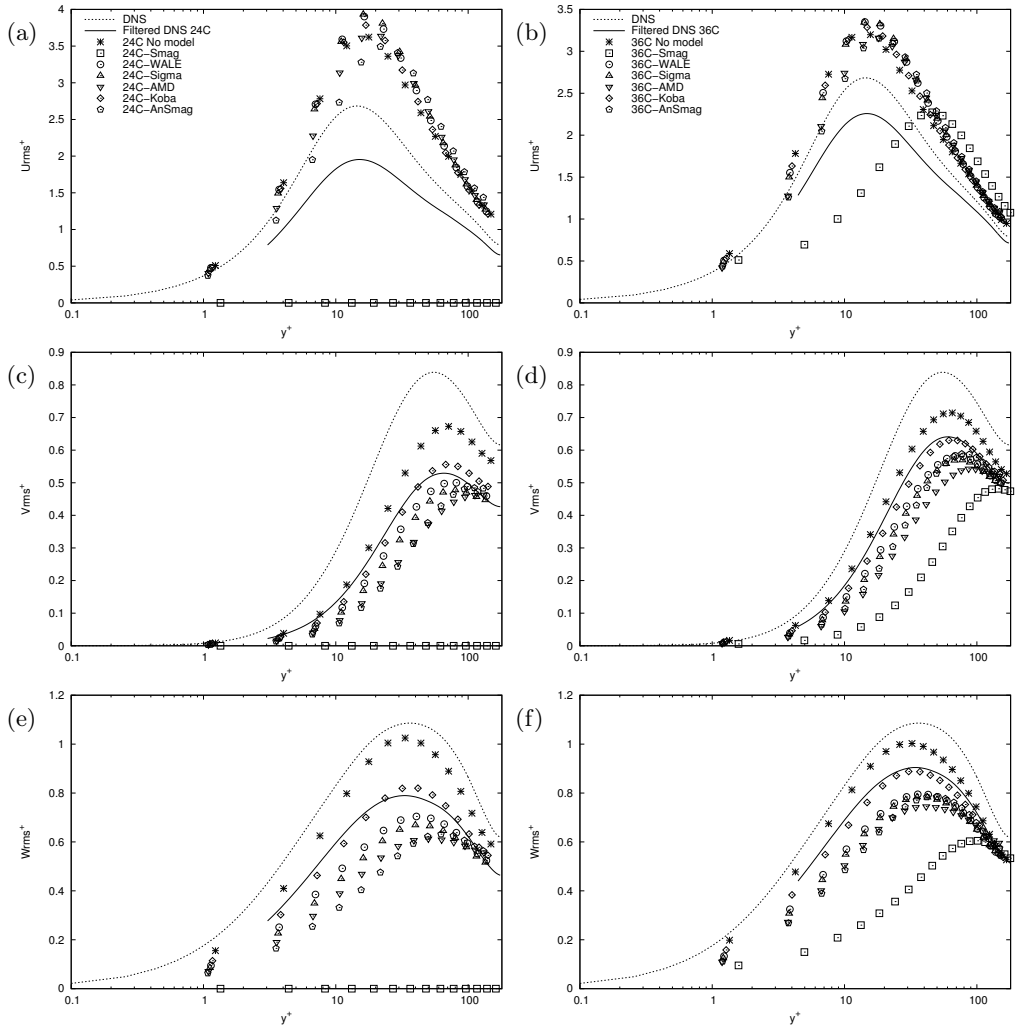

Figure 4 – Comparison of large-eddy simulations with the Smagorinsky, WALE, Sigma, AMD, Kobayashi and Anisotropic Smagorinsky models with the meshes 24C (left) and 36C (right) for the profiles of the standard deviation of streamwise velocity $\sqrt{\langle u_x'^2 \rangle}$ (a, b), wall-normal velocity $\sqrt{\langle u_y'^2 \rangle}$ (c, d) and spanwise velocity $\sqrt{\langle u_z'^2 \rangle}$ (e, f).

the Kobayashi model (figure 6(a)). This leads to more accurate results with the meshes and numerical method of this study.

Dynamic models provide a less arbitrary comparison of functional models in the sense that it is not complicated by the choice of the model parameter. We study plane-average, global-average, tensorial plane-average and tensorial global-average dynamic methods. The main purpose of the plane-average dynamic method is the local adaptation of the model parameter, which may compensate an unsatisfactory asymptotic near-wall behaviour of the model [65]. This is particularly well-suited to the Smagorinsky model. The plane-average dynamic Smagorinsky model (figure 5) gives similar results to the non-dynamic WALE and Sigma models. With the plane-average dynamic procedure, the Anisotropic Smagorinsky model deteriorates the predictions of the Smagorinsky model. Large-eddy simulations with the plane-average dynamic WALE, Sigma, AMD and Kobayashi models are not stable. This is consistent with the observation by Baya Toda *et al.* [6] that the plane-average dynamic method might degrade subgrid-scale models with a proper asymptotic near-wall

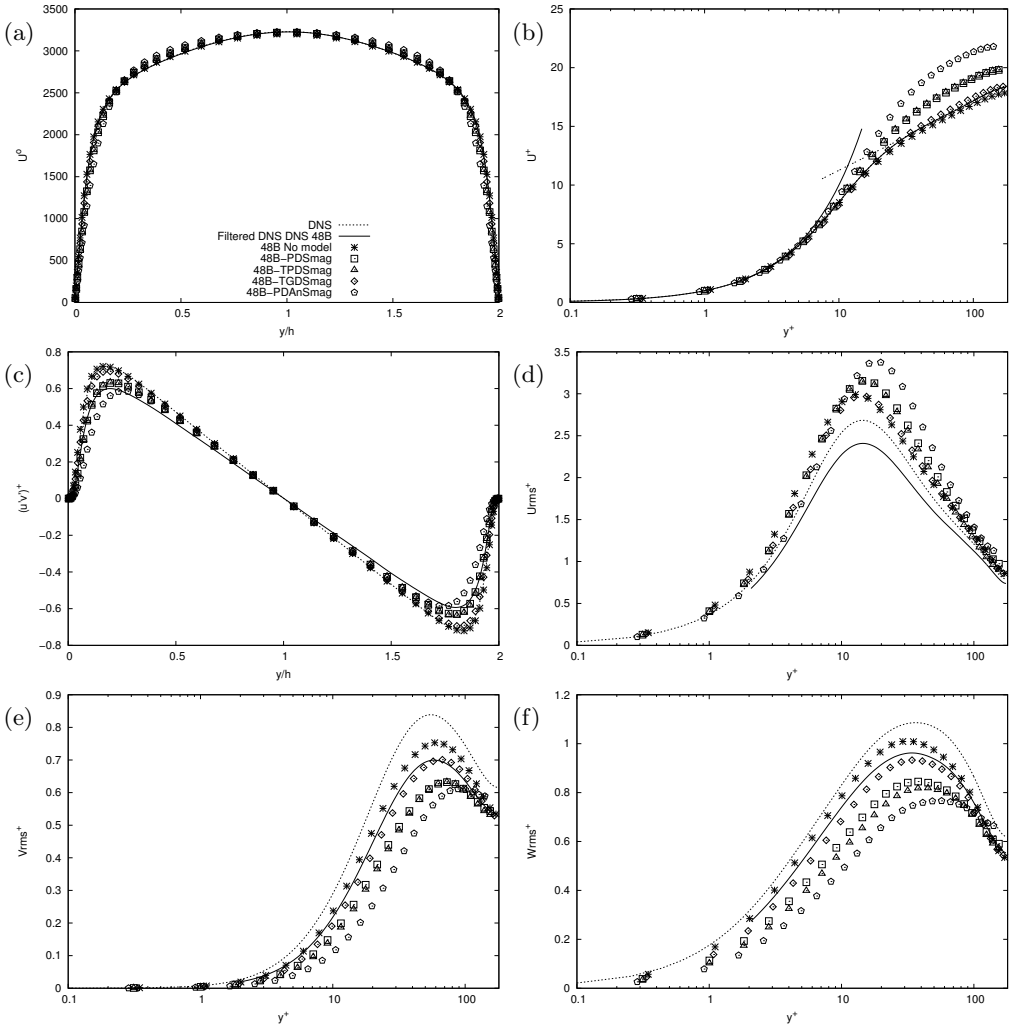

Figure 5 – Comparison of large-eddy simulations with the plane-average, tensorial plane-average and tensorial global-average dynamic Smagorinsky model and the plane-average dynamic Anisotropic Smagorinsky model for the profiles of the mean streamwise velocity $\langle U_x \rangle$ (a, b), the covariance of streamwise and wall-normal velocity $\langle u'_x u'_y \rangle$ (c), the standard deviation of streamwise velocity $\sqrt{\langle u'^2_x \rangle}$ (d), wall-normal velocity $\sqrt{\langle u'^2_y \rangle}$ (e) and spanwise velocity $\sqrt{\langle u'^2_z \rangle}$ (f) with the mesh 48B.

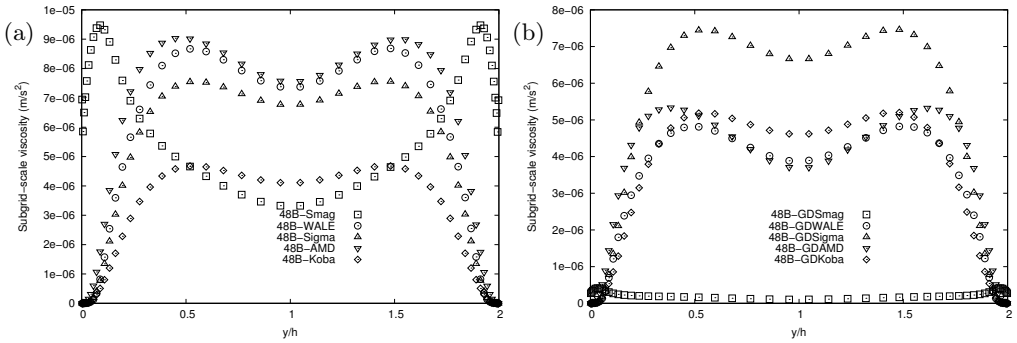

Figure 6 – Comparison of simulations with the constant-parameters and global-average dynamic Smagorinsky, WALE, Sigma, AMD, Kobayashi and Anisotropic Smagorinsky models for the profiles of the subgrid-scale viscosity with the mesh 48B.

	Average of the dynamic parameter (standard deviation), $\langle C^{\mathrm{mod}} \rangle$ ($\sqrt{\langle (C^{\mathrm{mod}})^2 \rangle - \langle C^{\mathrm{mod}} \rangle^2}$)		
	Mesh 24C	Mesh 36C	Mesh 48 B
Smag.	0.009 (0.001)	0.016 (0.001)	0.033 (0.001)
WALE	1.337 (0.554)	0.591 (0.073)	0.494 (0.038)
Sigma	1.723 (0.263)	1.182 (0.083)	0.982 (0.046)
AMD	—	—	0.455 (0.019)
Kobayashi	—	—	1.151 (0.088)
An. Smag.	0.694 (0.080)	1.008 (0.075)	1.544 (0.101)
Gradient	—	—	2.593 (0.053)

Table 2 – Average and normalised standard deviation of the dynamic parameter of the large-eddy simulations with the global-average dynamic Smagorinsky, WALE, Sigma, AMD, Kobayashi and Anisotropic Smagorinsky models with the meshes 24C, 36C and 48B.

	Average of the dynamic parameter (standard deviation), $\langle C^{\mathrm{mod}} \rangle$ ($\sqrt{\langle (C^{\mathrm{mod}})^2 \rangle - \langle C^{\mathrm{mod}} \rangle^2}$)					
	xx	xy	xz	yy	zy	zz
Smag.	6.755 (0.434)	0.028 (0.001)	0.073 (0.049)	0.269 (0.025)	−0.011 (0.005)	−0.266 (0.036)
WALE	−0.732 (0.159)	1.463 (0.093)	0.432 (0.041)	0.225 (0.066)	−0.035 (0.023)	0.418 (0.056)
Sigma	1.664 (0.267)	1.662 (0.077)	0.617 (0.069)	0.155 (0.058)	0.002 (0.030)	0.160 (0.050)
AMD	0.624 (0.097)	0.750 (0.035)	0.245 (0.038)	0.001 (0.034)	0.035 (0.022)	−0.064 (0.026)
Kobayashi	2.546 (0.274)	2.719 (0.175)	0.785 (0.133)	−0.145 (0.081)	0.048 (0.046)	−0.030 (0.067)
An. Smag.	5.435 (0.480)	1.618 (0.148)	0.275 (0.094)	1.531 (0.259)	−0.236 (0.086)	−0.323 (0.078)
Gradient	2.587 (0.061)	2.404 (0.039)	1.379 (0.039)	2.928 (0.067)	1.566 (0.041)	1.949 (0.031)

Table 3 – Average and normalised standard deviation of the dynamic parameters of the large-eddy simulations with the tensorial global-average dynamic Smagorinsky, WALE, Sigma, AMD, Kobayashi and Anisotropic Smagorinsky models with the mesh 48B.

behaviour and lead to numerical instabilities.

The global-average dynamic method multiplies the subgrid-scale models by a time-dependent function without modifying the local behaviour of the model. The average and standard deviation of the dynamic parameters are given in table 2. The global-average dynamic procedure increases the subgrid-scale viscosity of the Kobayashi and Anisotropic Smagorinsky models but reduces the subgrid-scale viscosity of the WALE and AMD models, except with the mesh 24C. The Smagorinsky model is made negligible to prevent its detrimental near-wall influence (figure 6(b)). The global-average dynamic WALE, AMD and Kobayashi models lead to a good prediction of the standard deviation of wall-normal and spanwise velocity, but the standard deviation of streamwise velocity is not improved compared to the no-model simulation (figure 7). The Sigma and Anisotropic Smagorinsky models do not provide good results with the global-average dynamic procedure.

The tensorial global-average dynamic method alters the relative contribution of each component of the subgrid-scale models. Excluding the Anisotropic Smagorinky model, the

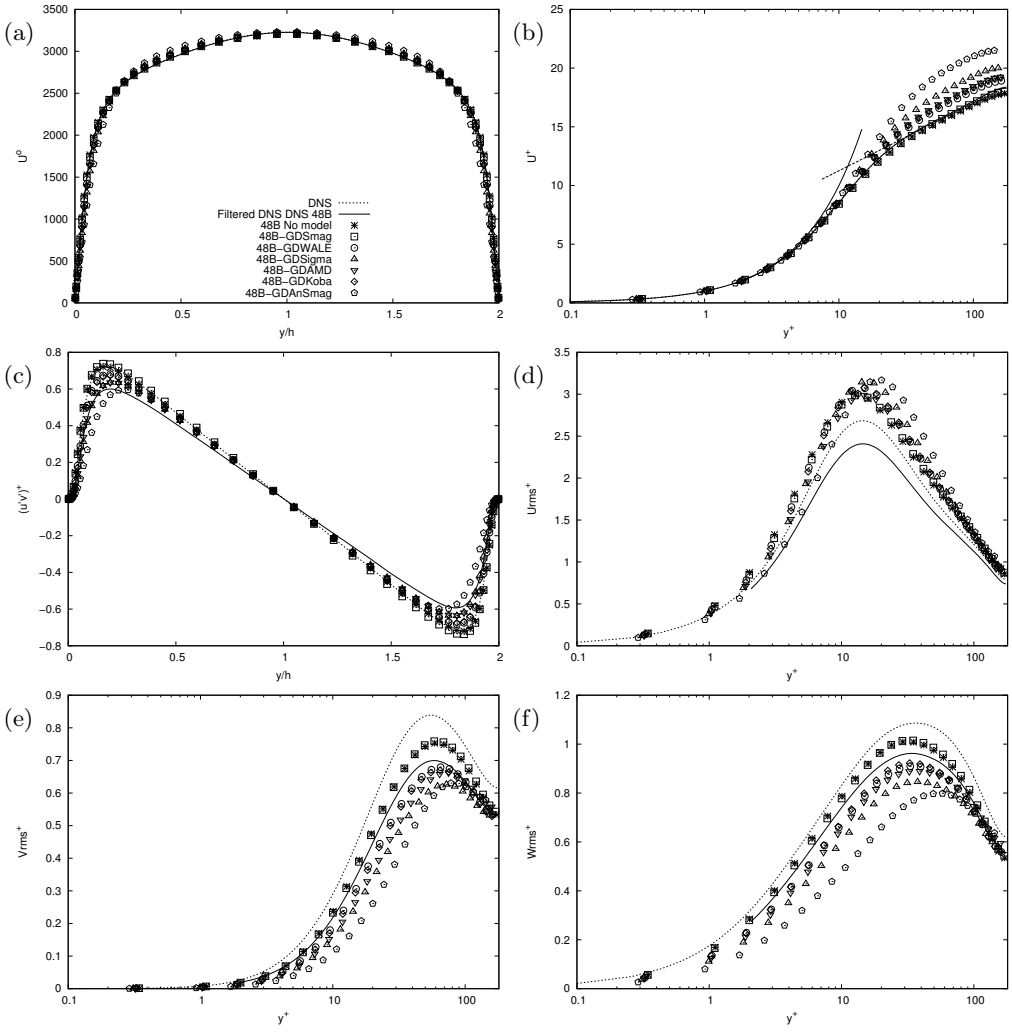

Figure 7 – Comparison of large-eddy simulations with the global-average dynamic Smagorinsky, WALE, Sigma, AMD, Kobayashi and Anisotropic Smagorinsky models for the profiles of the mean streamwise velocity $\langle U_x \rangle$ (a, b), the covariance of streamwise and wall-normal velocity $\langle u'_x u'_y \rangle$ (c), the standard deviation of streamwise velocity $\sqrt{\langle u'^2_x \rangle}$ (d), wall-normal velocity $\sqrt{\langle u'^2_y \rangle}$ (e) and spanwise velocity $\sqrt{\langle u'^2_z \rangle}$ (f) with the mesh 48B.

tensorial global-average dynamic procedure decreases heavily the relative amplitude of the "yy", "yz" and "zz" components, moderately decreases the "xz" component and amplifies the "xy" (table 3). The effect of the tensorial global-average dynamic procedure on the "xx" component is strongly dependent of the model. Depending on the model and the component, negative average parameters are obtained. In other words, the models are not purely dissipative. The Sigma model is the only functional model investigated with only positive parameters. The "xy" and "xz" are positive for all models while the "zz" component is negative for most models. The tensorial global-average dynamic Smagorinsky model decreases the standard deviation of wall-normal and spanwise velocity without increasing the standard deviation of streamwise velocity (figure 5). Similar results are obtained with the tensorial global-average dynamic WALE, AMD and Kobayashi models (figure 8). This is an improvement compared to the global-average dynamic procedure. The tensorial global-average dynamic AMD model is able to decrease the maximum value of the standard deviation of streamwise velocity, improving the results compared to the

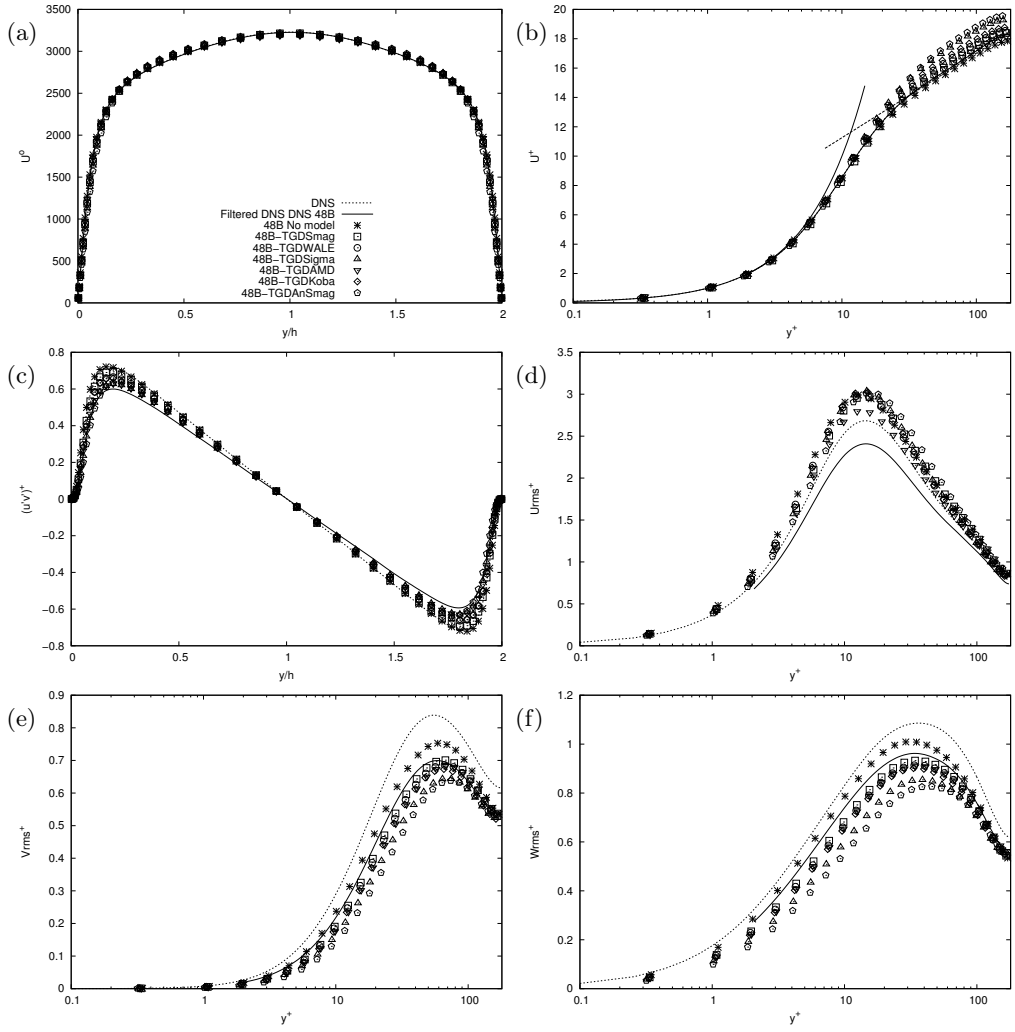

Figure 8 – Comparison of large-eddy simulations with the tensorial global-average dynamic Smagorinsky, WALE, Sigma, AMD, Kobayashi and Anisotropic Smagorinsky models for the profiles of the mean streamwise velocity $\langle U_x \rangle$ (a, b), the covariance of streamwise and wall-normal velocity $\langle u'_x u'_y \rangle$ (c), the standard deviation of streamwise velocity $\sqrt{\langle u'^2_x \rangle}$ (d), wall-normal velocity $\sqrt{\langle u'^2_y \rangle}$ (e) and spanwise velocity $\sqrt{\langle u'^2_z \rangle}$ (f) with the mesh 48B.

no-model simulation. It is the only investigated functional model with this property.

4.3 Structural modelling

In this section, we investigate the structural modelling of the subgrid-scale tensor. The structural models investigated are the gradient and scale-similarity models, as well as the dynamic versions of the gradient model. We give the results of large-eddy simulations with the gradient and scale-similarity models in figure 9 with the mesh 48B. The classical gradient model ($C^{\text{Grad.}} = 1$) improves slightly the standard deviation of streamwise velocity compared to the no-model simulation, but deteriorates the profiles of the standard deviation of wall-normal and spanwise velocity near the wall and the prediction of the wall shear stress. Nonetheless, the effects of the gradient model on the flow are rather small. To amplify the effects, we investigate gradient models with a parameter $C^{\text{Grad.}}$ larger than

one. The simulations are not stable using large multiplicative parameters. The filtering of the gradient model improves the stability of the simulation. The resulting filtered gradient model may be seen as an alternative formulation of the rational model proposed by Galdi and Layton [20][see also 8, 26, 27, 9],

$$\tau_{ij}^{\text{Grad,filtered}}(\boldsymbol{U},\overline{\boldsymbol{\Delta}}) = \widehat{\tau_{ij}^{\text{Grad.}}(\boldsymbol{U},\overline{\boldsymbol{\Delta}})} = \widehat{\tfrac{1}{12}C^{\text{Grad.}}\overline{\Delta}_k^2 g_{ik}g_{jk}}. \tag{34}$$

The test filter $\widehat{\cdot}$ is computed using filter A. The filtering alters the results of the simulation since with $C^{\text{Grad.}} = 2$, the predicted wall shear stress is significantly different for the nonfiltered and filtered gradient models (figure 9). With $C^{\text{Grad.}} = 9$, the filtered gradient model leads to a standard deviation of streamwise velocity at the level of the filtered direct numerical simulation. However, the covariance of streamwise and wall-normal velocity and the standard deviation of wall-normal and spanwise velocity are underestimated. Hence, there is no Pareto improvement compared to the classical gradient model.

The plane-average and global-average dynamic gradient models give nearly identical results because the plane-average dynamic parameter does not strongly depend on the wall-normal coordinate (figure 10). They amplify on average the gradient model (table 2) and provide similar results to the constant-parameter simulations. The tensorial plane-average or global-average dynamic gradient model amplify each component of the gradient model but increase in particular the relative amplitude of the "xx", "xy" and "yy" components (table 3). The tensorial dynamic gradient models, and the plane-average dynamic gradient model in particular, provide a more accurate prediction of the wall shear stress and the near-wall profile of the standard deviation of wall-normal and spanwise velocity (figure 10).

The results of the large-eddy simulations with the scale-similarity model depend on the filter used (figure 9). Using filter A, the scale-similarity model is tied to the gradient model with $C^{\text{Grad.}} = 9$ according to the Taylor series expansion (13) of the test filter in the scale-similarity model with $\widehat{\overline{\Delta}}_k^2 \approx 3\overline{\Delta}_k$. Using filter T, the scale-similarity model is tied to the gradient model with $C^{\text{Grad.}} = 1$ since $\widehat{\overline{\Delta}}_k^2 \approx \overline{\Delta}_k$. However, the predictions with the scale-similarity and gradient model are not the same, suggesting that the higher-order terms are relevant. With the filter A, the scale-similarity model has with the mesh 48B an excessive impact on the flow and deteriorates the profiles of the turbulence statistics. With the filter T, the model is more similar to the original model of Bardina *et al.* [5]. The prediction of all turbulence statistics is with the mesh 48B improved compared to the no-model simulation. In particular, the covariance of streamwise and wall-normal velocity and the standard deviation of wall-normal and spanwise velocity are in agreement with the filtered direct numerical simulation. The standard deviation of wall-normal and spanwise velocity remains overestimated but is decreased compared to the no-model simulation. These satisfactory results do not generalise very well to the 24C and 36C meshes. Indeed, the effects of the scale-similarity model on the turbulence statistics is similar for the three meshes and does not seem to correctly take into account the variations of filter width. As a result, the covariance of streamwise and wall-normal velocity and the standard deviation of velocity components are overestimated with the meshes 24C and 36C (figure 11).

4.4 Tensorial models and tensorial mixed models

In this section, we investigate the modelling of the subgrid-scale tensor with tensorial, mixed and tensorial mixed models, as well as the dynamic versions of these models. We focus in particular on models based on the AMD model. The results of large-eddy simulations with various tensorial AMD models is compared in figure 12 with the mesh 48B. The

models based on the $H^{(4)}$ (equation 18) tensor leads to the best prediction of the wall shear stress while those based on the $H^{(2)}$ (equation 16), $H^{(3)}$ (equation 17) and $H^{(6)}$ (equation 20) tensors heavily underestimate or overestimate the wall shear stress. Compared to the classical AMD model, the tensorial AMD models based on the $H^{(2)}$ (equation 16), $H^{(4)}$ (equation 18) and $H^{(5)}$ (equation 19) tensors give better predictions of the covariance of streamwise and wall-normal velocity and of the standard deviation of velocity components. Besides, while functional models were found unable to decrease the maximum value of the standard deviation of streamwise velocity compared to the no-model simulation (figure 3), all tensorial AMD models investigated verify this property. The behaviour of the tensorial AMD models upon mesh derefinement is as the scale-similarity model not satisfactory for the covariance of streamwise and wall-normal velocity and the standard deviation of streamwise velocity. Indeed, the reduction of the maximum amplitude is not sufficiently enhanced with the coarser meshes (figure 15). It is however more acceptable for the standard deviation of wall-normal and spanwise velocity in the sense that the profiles undergo the expected decrease of maximum amplitude with increased filter width.

Contrary to tensorial AMD models, the tensorial models based on the Smagorinsky, WALE or Sigma model do not decrease the maximum value standard deviation of streamwise velocity with the mesh 48B (figure 14). A decrease is also obtained using a tensorial Anistropic Smagorinsky model, but the effect is smaller than with the AMD model. While the underlying explication is not known, this is to some extent consistent with the results of tensorial global-average dynamic models (figure 8), in which the AMD model led to a stronger decrease of the standard deviation of streamwise velocity.

Tensorial gradient-AMD mixed models complement tensorial AMD models using the gradient model to close the components of the subgrid term not modelled by the AMD model. The addition of the gradient model to the AMD model has only a small effect on the turbulence statistics (figure 13). It decreases the estimated wall shear stress, providing an improvement for the classical AMD model and the tensorial AMD models based on the $H^{(1)}$ (equation 15), $H^{(3)}$ (equation 17), $H^{(4)}$ (equation 18) and $H^{(6)}$ (equation 20) tensors, which overestimate the wall shear stress, and a degradation for the tensorial AMD models based on the $H^{(2)}$ (equation 16) and $H^{(5)}$ (equation 19) tensors, which underestimate the wall shear stress.

We investigated various dynamic versions of gradient-AMD mixed models. Dynamic gradient-AMD mixed models may be based on a plane average, a global average, a tensorial plane average or a tensorial global average. Some dynamic procedures are not stable. The stability of the dynamic procedures investigated is reported in table 4. Plane-average dynamic methods are only stable if the AMD-related part of the model is not dynamic. Global-average dynamic methods are more stable. All dynamic procedures investigated are stable if the negative values of the dynamic parameters of the AMD model are clipped. However, this makes the AMD model negligible using a global average (table 5) or a tensorial global average (table 6). If the dynamic procedure is not tensorial, the one-parameter dynamic method based on the prior computation of the AMD model with the classical dynamic procedure (P1Grad+PDAMD or G1Grad+GDAMD) and the two-parameter dynamic method (P2(Grad+AMD) or G2(Grad+AMD)) give similar results. The one-parameter dynamic method based on the prior computation of the gradient model with the classical dynamic method (PDGrad+P1AMD or GDGrad+G1AMD) and the use of the classical dynamic method for the gradient and AMD models (PDGrad+PDAMD or GDGrad+GDAMD) also give similar results. We compare in figure 16 a selection of the best-performing models for each type of dynamic procedure. The dynamic gradient-AMD

	Type of averaging	Dynamic method of each model Gradient	AMD	Stability
P1Grad+AMD	Plane-average	One-parameter	Not dynamic	Stable
PDGrad+PDAMD	Plane-average	Classical	Classical	Not stable
PDGrad+P1AMD	Plane-average	Classical	One-parameter	Not stable
P1Grad+PDAMD	Plane-average	One-parameter	Classical	Not stable
P2(Grad+AMD)	Plane-average	Two-parameter	Two-parameter	Not stable
TP1Grad+AMD	Tensorial plane-average	One-parameter	Not dynamic	Stable
TPDGrad+TPDAMD	Tensorial plane-average	Classical	Classical	Not stable
TPDGrad+TP1AMD	Tensorial plane-average	Classical	One-parameter	Not stable
TP1Grad+TPDAMD	Tensorial plane-average	One-parameter	Classical	Not stable
TP2(Grad+AMD)	Tensorial plane-average	Two-parameter	Two-parameter	Not stable
G1Grad+AMD	Global-average	One-parameter	Not dynamic	Stable
GDGrad+GDAMD	Global-average	Classical	Classical	Stable
GDGrad+G1AMD	Global-average	Classical	One-parameter	Stable
G1Grad+GDAMD	Global-average	One-parameter	Classical	Not stable
G2(Grad+AMD)	Global-average	Two-parameter	Two-parameter	Not stable
TG1Grad+AMD	Tensorial global-average	One-parameter	Not dynamic	Stable
TGDGrad+TGDAMD	Tensorial global-average	Classical	Classical	Stable
TGDGrad+TG1AMD	Tensorial global-average	Classical	One-parameter	Not stable
TG1Grad+TGDAMD	Tensorial global-average	One-parameter	Classical	Stable
TG2(Grad+AMD)	Tensorial global-average	Two-parameter	Two-parameter	Not stable

Table 4 – Stability of the large-eddy simulations with plane-average, global-average, tensorial plane-average and tensorial global-average dynamic methods for gradient-AMD mixed models with the mesh 48B. The clipping only concerns the negative dynamic parameters of the AMD model.

mixed models do not provide significant improvements over the constant-parameter tensorial gradient-AMD mixed models. The best results are achieved with tensorial dynamic procedures.

All in all, while none of the models investigated is able to properly reproduce the effect of the subgrid-scale tensor on the flow, some models improves the predictions of the simulation compared to the no-model case. We recommend the use of the scale-similarity model and the constant-parameter or dynamic tensorial AMD model, which provide the most promising results.

5 Conclusion

Subgrid-scale models are investigated using large-eddy simulations of a fully developed turbulent channel flow. The large-eddy simulations implementing the models are carried out using a finite method in a staggered grid system with a third-order Runge–Kutta time scheme. To examine the influence of the modelling, the large-eddy simulations are compared to a filtered direct numerical simulation. The modelling of the subgrid-scale tensor governs the wall shear stress and the turbulence anisotropy. The gradient model is not sufficiently impactful in a large-eddy simulation and must be filtered and amplified to al-

	Average of the dynamic parameter (standard deviation), $\langle C^{\mathrm{mod}} \rangle$ ($\sqrt{\langle (C^{\mathrm{mod}})^2 \rangle - \langle C^{\mathrm{mod}} \rangle^2}$)	
	AMD-related	Gradient-related
G1Grad+AMD	—	1.760 (0.047)
GDGrad+GDAMD	0.424 (0.017)	2.245 (0.054)
GDGrad+G1AMD	0.424 (0.017)	2.208 (0.053)
G1Grad+GDAMD*	0.003 (0.007)	2.587 (0.053)
G2(Grad+AMD)*	0.003 (0.008)	2.589 (0.054)

Table 5 – Average and normalised standard deviation of the AMD-related and gradient-related dynamic parameters of the large-eddy simulations with global-average dynamic gradient-AMD mixed models with the mesh 48B. An asterisk (*) indicates the clipping of the AMD-related part.

	Average of the dynamic parameter (standard deviation), $\langle C^{\mathrm{mod}} \rangle$ ($\sqrt{\langle (C^{\mathrm{mod}})^2 \rangle - \langle C^{\mathrm{mod}} \rangle^2}$)					
	xx	xy	xz	yy	zy	zz
TG1Grad+AMD	—	—	—	—	—	—
TGDGrad+TGDAMD	0.634 (0.080)	0.761 (0.031)	0.255 (0.037)	−0.020 (0.033)	0.049 (0.021)	−0.076 (0.025)
TGDGrad+TG1AMD*	0.000 (0.000)	0.213 (0.019)	0.125 (0.022)	0.100 (0.022)	0.003 (0.005)	0.000 (0.000)
TG1Grad+TGDAMD	0.584 (0.076)	0.799 (0.033)	0.258 (0.038)	−0.008 (0.034)	0.050 (0.021)	−0.073 (0.025)
TG2(Grad+AMD)*	0.000 (0.000)	0.327 (0.030)	0.121 (0.022)	0.101 (0.023)	0.003 (0.005)	0.000 (0.000)

(a) AMD-related dynamic parameters

	Average of the dynamic parameter (standard deviation), $\langle C^{\mathrm{mod}} \rangle$ ($\sqrt{\langle (C^{\mathrm{mod}})^2 \rangle - \langle C^{\mathrm{mod}} \rangle^2}$)					
	xx	xy	xz	yy	zy	zz
TG1Grad+AMD	1.818 (0.051)	0.465 (0.070)	1.244 (0.053)	2.326 (0.077)	1.466 (0.060)	1.668 (0.049)
TGDGrad+TGDAMD	2.280 (0.053)	2.271 (0.060)	1.422 (0.034)	2.681 (0.067)	1.598 (0.034)	1.853 (0.030)
TGDGrad+TG1AMD*	2.473 (0.056)	2.359 (0.060)	1.408 (0.037)	2.840 (0.066)	1.599 (0.038)	1.933 (0.030)
TG1Grad+TGDAMD	2.311 (0.055)	1.302 (0.048)	1.388 (0.035)	2.727 (0.068)	1.587 (0.035)	1.875 (0.029)
TG2(Grad+AMD)*	2.486 (0.057)	1.962 (0.061)	1.399 (0.037)	2.863 (0.067)	1.601 (0.039)	1.940 (0.031)

(b) Gradient-related dynamic parameters

Table 6 – Average and normalised standard deviation of the AMD-related and gradient-related dynamic parameters of the large-eddy simulations with tensorial global-average dynamic gradient-AMD mixed models with the mesh 48B. An asterisk (*) indicates the clipping of the AMD-related part.

ters significantly the flow. Functional eddy-viscosity models do not accurately represent the turbulence anisotropy as the standard deviation of streamwise velocity is insufficiently decreased compared to the wall-normal and spanwise components. Scalar dynamic procedures avoid the need for an arbitrary model parameter but does not improve significantly the prediction of models with a proper asymptotic near-wall behaviour. On the other hand, tensorial eddy-viscosity models can provide more accurate predictions of the wall shear stress and the turbulence anisotropy than scalar eddy-viscosity models using either a constant tensorial coefficient or a tensorial dynamic procedure. The effects are particularly salient with the AMD model.

Acknowledgments

This work was funded by the French Investments for the future ("Investissements d'Avenir") programme managed by the National Agency for Research (ANR) under contract ANR-10-LABX-22-01 (labex SOLSTICE). The authors gratefully acknowledge the CEA for the development of the TRUST platform. This work was granted access to the HPC resources of CINES under the allocations 2017-A0022A05099 and 2018-A0042A05099 made by GENCI.

References

[1] A. Abba, A. C. Cercignani, and L. Valdettaro. Analysis of subgrid scale models. *Comput. Math. Appl.*, 46(4):521–535, 2003.

[2] A. Abba, L. Bonaventura, M. Nini, and M. Restelli. Dynamic models for large eddy simulation of compressible flows with a high order dg method. *Computers & Fluids*, 122:209–222, 2015.

[3] R. Anderson and C. Meneveau. Effects of the similarity model in finite-difference les of isotropic turbulence using a lagrangian dynamic mixed model. *Flow, Turbulence and Combustion*, 62(3):201–225, 1999.

[4] F. Aulery, D. Dupuy, A. Toutant, F. Bataille, and Y. Zhou. Spectral analysis of turbulence in anisothermal channel flows. *Computers & Fluids*, 151:115–131, 2017.

[5] J. Bardina, J. Ferziger, and W. C. Reynolds. Improved subgrid-scale models for large-eddy simulation. In *13th Fluid and Plasma Dynamics Conference*, page 1357, 1980.

[6] H. Baya Toda, O. Cabrit, G. Balarac, S. Bose, J. Lee, H. Choi, and F. Nicoud. A subgrid-scale model based on singular values for les in complex geometries. In *Proc. of the Summer Program*, pages 193–202, 2010.

[7] H. Baya Toda, K. Truffin, and F. Nicoud. Is the dynamic procedure appropriate for all sgs models. In *V European Conference on Computational Fluid Dynamics, ECCOMAS, Lisbon, Portugal*, pages 14–17, 2010.

[8] L. C. Berselli, G. P. Galdi, T. Iliescu, and W. J. Layton. Mathematical analysis for the rational large eddy simulation model. *Mathematical Models and Methods in Applied Sciences*, 12(08): 1131–1152, 2002.

[9] L. C. Berselli, T. Iliescu, and W. J. Layton. *Mathematics of large eddy simulation of turbulent flows*. Springer Science & Business Media, 2005.

[10] I. A. Bolotnov, R. T. Lahey, D. A. Drew, K. E. Jansen, and A. A. Oberai. Spectral analysis of turbulence based on the DNS of a channel flow. *Computers & Fluids*, 39(4):640–655, 2010.

[11] J. Boussinesq. *Essai sur la théorie des eaux courantes*. Impr. nationale, 1877.

[12] C. Calvin, O. Cueto, and P. Emonot. An object-oriented approach to the design of fluid mechanics software. *ESAIM: Mathematical Modelling and Numerical Analysis*, 36(05):907–921, 2002.

[13] S. Chen, Z. Xia, S. Pei, J. Wang, Y. Yang, Z. Xiao, and Y. Shi. Reynolds-stress-constrained large-eddy simulation of wall-bounded turbulent flows. *Journal of Fluid Mechanics*, 703:1–28, 2012.

[14] J. W. Deardorff. A numerical study of three-dimensional turbulent channel flow at large reynolds numbers. *Journal of Fluid Mechanics*, 41(2):453–480, 1970.

[15] F. Denaro, A. Abba, M. Germano, M. Icardi, D. Marchisio, S. Rolfo, P. Lampitella, E. Colombo, F. Inzoli, A. Aprovitola, F. S. Marra, M. Ioveno, and D. Tordella. A comparative test for assessing the performances of large-eddy simulation codes. In *AIMETA Conference*, 2011.

[16] D. Dupuy, A. Toutant, and F. Bataille. Study of the large-eddy simulation subgrid terms of a low mach number anisothermal channel flow. *International Journal of Thermal Sciences*, 135:221–234, 2018.

[17] D. Dupuy, A. Toutant, and F. Bataille. Turbulence kinetic energy exchanges in flows with highly variable fluid properties. *Journal of Fluid Mechanics*, 834:5–54, 2018.

[18] D. Dupuy, A. Toutant, and F. Bataille. A priori tests of subgrid-scale models in an anisothermal turbulent channel flow at low mach number. *International Journal of Thermal Sciences*, 145:105999, 2019.

[19] D. Dupuy, A. Toutant, and F. Bataille. Effect of the reynolds number on turbulence kinetic energy exchanges in flows with highly variable fluid properties. *Physics of Fluids*, 31(1): 015104, 2019.

[20] G. P. Galdi and W. J. Layton. Approximation of the larger eddies in fluid motions ii: A model for space-filtered flow. *Mathematical Models and Methods in Applied Sciences*, 10(03): 343–350, 2000.

[21] M. Germano. Turbulence: the filtering approach. *Journal of Fluid Mechanics*, 238:325–336, 1992.

[22] M. Germano, U. Piomelli, P. Moin, and W. H. Cabot. A dynamic subgrid-scale eddy viscosity model. *Physics of Fluids A: Fluid Dynamics*, 3(7):1760–1765, 1991.

[23] N. S. Ghaisas and S. H. Frankel. Dynamic gradient models for the sub-grid scale stress tensor and scalar flux vector in large eddy simulation. *Journal of Turbulence*, 17(1):30–50, 2016.

[24] H. Gopalan, S. Heinz, and M. K. Stöllinger. A unified rans–les model: Computational development, accuracy and cost. *Journal of Computational Physics*, 249:249–274, 2013.

[25] K. Horiuti. A new dynamic two-parameter mixed model for large-eddy simulation. *Physics of Fluids*, 9(11):3443–3464, 1997.

[26] T. Iliescu and P. Fischer. Large eddy simulation of turbulent channel flows by the rational large eddy simulation model. *Physics of Fluids*, 15(10):3036–3047, 2003.

[27] T. Iliescu and P. Fischer. Backscatter in the rational les model. *Computers & Fluids*, 33(5-6): 783–790, 2004.

[28] H. Jeanmart and G. Winckelmans. Investigation of eddy-viscosity models modified using discrete filters: a simplified "regularized variational multiscale model" and an "enhanced field model". *Physics of Fluids*, 19(5):055110, 2007.

[29] Z. Jiang, Z. Xiao, Y. Shi, and S. Chen. Constrained large-eddy simulation of wall-bounded compressible turbulent flows. *Physics of Fluids*, 25(10):106102, 2013.

[30] Z. Jiang, Z. Xia, Y. Shi, and S. Chen. Large-eddy simulation of plane channel flow with vreman's model. *Journal of Turbulence*, 17(8):807–822, 2016.

[31] Z. Jiang, Z. Xia, Y. Shi, and S. Chen. Large eddy simulation of spanwise rotating turbulent channel flow with dynamic variants of eddy viscosity model. *Physics of Fluids*, 30(4):040909, 2018.

[32] J. Jiménez. The physics of wall turbulence. *Physica A: Statistical Mechanics and its Applications*, 263(1-4):252–262, 1999.

[33] J. Jiménez. Near-wall turbulence. *Physics of Fluids*, 25(10):101302, 2013.

[34] H. Kobayashi. The subgrid-scale models based on coherent structures for rotating homogeneous turbulence and turbulent channel flow. *Physics of Fluids*, 17(4):045104, 2005.

[35] P. Lampitella. *Large eddy simulation for complex industrial flows*. PhD thesis, Italy, 2014.

[36] J. Larsson, S. Kawai, J. Bodart, and I. Bermejo-Moreno. Large eddy simulation with modeled wall-stress: recent progress and future directions. *Mechanical Engineering Reviews*, 3(1): 15–00418, 2016.

[37] J. Lee, H. Choi, and N. Park. Dynamic global model for large eddy simulation of transient flow. *Physics of Fluids*, 22(7):075106, 2010.

[38] M. Lee and R. D. Moser. Direct numerical simulation of turbulent channel flow up to $\mathrm{Re}_\tau \approx 5200$. *Journal of Fluid Mechanics*, 774:395–415, 2015.

[39] A. Leonard. Energy cascade in large eddy simulations of turbulent fluid flows. *Advances in Geophysics*, 18A:237–248, 1974.

[40] D. K. Lilly. A proposed modification of the germano subgrid-scale closure method. *Physics of Fluids A: Fluid Dynamics*, 4(3):633–635, 1992.

[41] H. Lu and C. J. Rutland. Structural subgrid-scale modeling for large-eddy simulation: A review. *Acta Mechanica Sinica*, 32(4):567–578, 2016.

[42] R. Mathis, N. Hutchins, and I. Marusic. Large-scale amplitude modulation of the small-scale structures in turbulent boundary layers. *Journal of Fluid Mechanics*, 628:311–337, 2009.

[43] J. Meyers and P. Sagaut. Is plane-channel flow a friendly case for the testing of large-eddy simulation subgrid-scale models? *Physics of Fluids*, 19(4):048105, 2007.

[44] R. Mokhtarpoor and S. Heinz. Dynamic large eddy simulation: Stability via realizability. *Physics of Fluids*, 29(10):105104, 2017.

[45] R. Mokhtarpoor, S. Heinz, and M. Stoellinger. Dynamic unified rans-les simulations of high reynolds number separated flows. *Physics of Fluids*, 28(9):095101, 2016.

[46] Y. Morinishi and O. V. Vasilyev. A recommended modification to the dynamic two-parameter mixed subgrid scale model for large eddy simulation of wall bounded turbulent flow. *Physics of Fluids*, 13(11):3400–3410, 2001.

[47] Y. Morinishi, T. S. Lundhomas, O. V. Vasilyev, and P. Moin. Fully conservative higher order finite difference schemes for incompressible flow. *Journal of Computational Physics*, 143(1): 90–124, 1998.

[48] R. D. Moser, J. Kim, and N. N. Mansour. Direct numerical simulation of turbulent channel flow up to $\mathrm{Re}_\tau = 590$. *Physics of Fluids*, 11(4):943–945, 1999.

[49] F. Nicoud. Conservative high-order finite-difference schemes for low-Mach number flows. *Journal of Computational Physics*, 158(1):71–97, 2000.

[50] F. Nicoud and F. Ducros. Subgrid-scale stress modelling based on the square of the velocity gradient tensor. *Flow, Turbulence and Combustion*, 62(3):183–200, 1999. ISSN 1386-6184.

[51] F. Nicoud, H. Baya Toda, O. Cabrit, S. Bose, and J. Lee. Using singular values to build a subgrid-scale model for large eddy simulations. *Physics of Fluids*, 23(8):085106, 2011.

[52] M. Oberlack. Symmetries and invariant solutions of turbulent flows and their implications for turbulence modelling. In *Theories of Turbulence*, pages 301–366. Springer, 2002.

[53] T. Ohtsuka and K. Abe. Toward the development of an anisotropy-resolving subgrid-scale model for large eddy simulation. *Journal of Fluid Science and Technology*, 9(1):JFST0004–JFST0004, 2014.

[54] N. Park, S. Lee, J. Lee, and H. Choi. A dynamic subgrid-scale eddy viscosity model with a global model coefficient. *Physics of Fluids*, 18(12):125109, 2006.

[55] S. B. Pope. Ten questions concerning the large-eddy simulation of turbulent flows. *New Journal of Physics*, 6(1):35, 2004.

[56] D. Razafindralandy, A. Hamdouni, and M. Oberlack. Analysis and development of subgrid turbulence models preserving the symmetry properties of the navier–stokes equations. *European Journal of Mechanics-B/Fluids*, 26(4):531–550, 2007.

[57] M. Rieth, F. Proch, O. T. Stein, M. W. A. Pettit, and A. M. Kempf. Comparison of the sigma and smagorinsky les models for grid generated turbulence and a channel flow. *Computers & Fluids*, 99:172–181, 2014.

[58] W. Rozema, H.J. Bae, P. Moin, and R. Verstappen. Minimum-dissipation models for large-eddy simulation. *Physics of Fluids*, 27(8):085107, 2015.

[59] S. Ryu and G. Iaccarino. A subgrid-scale eddy-viscosity model based on the volumetric strain-stretching. *Physics of Fluids*, 26(6):065107, 2014.

[60] P. Sagaut. *Large eddy simulation for incompressible flows: an introduction*. Springer Science & Business Media, 2006.

[61] P. Sagaut, E. Garnier, and M. Terracol. A general algebraic formulation for multi-parameter dynamic subgrid-scale modeling. *International Journal of Computational Fluid Dynamics*, 13 (3):251–257, 2000.

[62] M. V. Salvetti and S. Banerjee. A priori tests of a new dynamic subgrid-scale model for finite-difference large-eddy simulations. *Physics of Fluids*, 7(11):2831–2847, 1995.

[63] M. V. Salvetti, Y. Zang, R. L. Street, and S. Banerjee. Large-eddy simulation of free-surface decaying turbulence with dynamic subgrid-scale models. *Physics of Fluids*, 9(8):2405–2419, 1997.

[64] F. Sarghini, U. Piomelli, and E. Balaras. Scale-similar models for large-eddy simulations. *Physics of Fluids*, 11(6):1596–1607, 1999.

[65] M. H. Silvis, R. A. Remmerswaal, and R. Verstappen. Physical consistency of subgrid-scale models for large-eddy simulation of incompressible turbulent flows. *Physics of Fluids*, 29(1): 015105, 2017.

[66] S. Singh and D. You. A dynamic global-coefficient mixed subgrid-scale model for large-eddy simulation of turbulent flows. *International Journal of Heat and Fluid Flow*, 42:94–104, 2013.

[67] J. Smagorinsky. General circulation experiments with the primitive equations: I. the basic experiment. *Monthly Weather Review*, 91(3):99–164, 1963.

[68] P. R. Spalart. Comments on the feasibility of les for wings, and on hybrid rans/les approach. In *Proceedings of First AFOSR International Conference on DNS/LES, 1997*, 1997.

[69] P. R. Spalart. Detached-eddy simulation. *Annual Review of Fluid Mechanics*, 41:181–202, 2009.

[70] C. G. Speziale. Galilean invariance of subgrid-scale stress models in the large-eddy simulation of turbulence. *Journal of Fluid Mechanics*, 156:55–62, 1985.

[71] S. Stolz, N. A. Adams, and L. Kleiser. An approximate deconvolution model for large-eddy simulation with application to incompressible wall-bounded flows. *Physics of Fluids*, 13(4): 997–1015, 2001.

[72] M. Strelets. Detached eddy simulation of massively separated flows. In *39th Aerospace sciences meeting and exhibit*, page 879, 2001.

[73] A. Toutant and F. Bataille. Turbulence statistics in a fully developed channel flow submitted to a high temperature gradient. *International Journal of Thermal Sciences*, 74:104–118, 2013.

[74] A. Travin, M. Shur, M. Strelets, and P. Spalart. Detached-eddy simulations past a circular cylinder. *Flow, Turbulence and Combustion*, 63(1-4):293–313, 2000.

[75] F. X. Trias, D. Folch, A. Gorobets, and A. Oliva. Building proper invariants for eddy-viscosity subgrid-scale models. *Physics of Fluids*, 27(6):065103, 2015.

[76] F. X. Trias, A. Gorobets, M. H. Silvis, R. W. C. P Verstappen, and A. Oliva. A new subgrid characteristic length for turbulence simulations on anisotropic grids. *Physics of Fluids*, 29 (11):115109, 2017.

[77] R. Verstappen. When does eddy viscosity damp subfilter scales sufficiently? *Journal of Scientific Computing*, 49(1):94, 2011.

[78] A. W. Vreman. An eddy-viscosity subgrid-scale model for turbulent shear flow: Algebraic theory and applications. *Physics of Fluids*, 16(10):3670–3681, 2004.

[79] A. W. Vreman and J. G. M. Kuerten. Comparison of direct numerical simulation databases of turbulent channel flow at $\mathrm{Re}_\tau = 180$. *Physics of Fluids*, 26(1):015102, 2014.

[80] B. Vreman, B. Geurts, and H. Kuerten. On the formulation of the dynamic mixed subgrid-scale model. *Physics of Fluids*, 6(12):4057–4059, 1994.

[81] J. H. Williamson. Low-storage Runge-Kutta schemes. *Journal of Computational Physics*, 35 (1):48–56, 1980.

[82] G. S. Winckelmans, H. Jeanmart, and D. Carati. On the comparison of turbulence intensities from large-eddy simulation with those from experiment or direct numerical simulation. *Physics of Fluids*, 14(5):1809–1811, 2002.

[83] D. You and P. Moin. A dynamic global-coefficient subgrid-scale eddy-viscosity model for large-eddy simulation in complex geometries. *Physics of Fluids*, 19(6):065110, 2007.

[84] C. Yu, Z. Xiao, and X. Li. Scale-adaptive subgrid-scale modelling for large-eddy simulation of turbulent flows. *Physics of Fluids*, 29(3):035101, 2017.

[85] Y. Zang, R. L. Street, and J. R. Koseff. A dynamic mixed subgrid-scale model and its application to turbulent recirculating flows. *Physics of Fluids A: Fluid Dynamics*, 5(12): 3186–3196, 1993.

[86] Y. Zhou. Rayleigh–taylor and richtmyer–meshkov instability induced flow, turbulence, and mixing. i. *Physics Reports*, 720-722:1–136, 2017.

[87] Y. Zhou. Rayleigh–taylor and richtmyer–meshkov instability induced flow, turbulence, and mixing. ii. *Physics Reports*, 723-725:1–160, 2017.

[88] Z. Zhou, S. Wang, and G. Jin. A structural subgrid-scale model for relative dispersion in large-eddy simulation of isotropic turbulent flows by coupling kinematic simulation with approximate deconvolution method. *Physics of Fluids*, 30(10):105110, 2018.

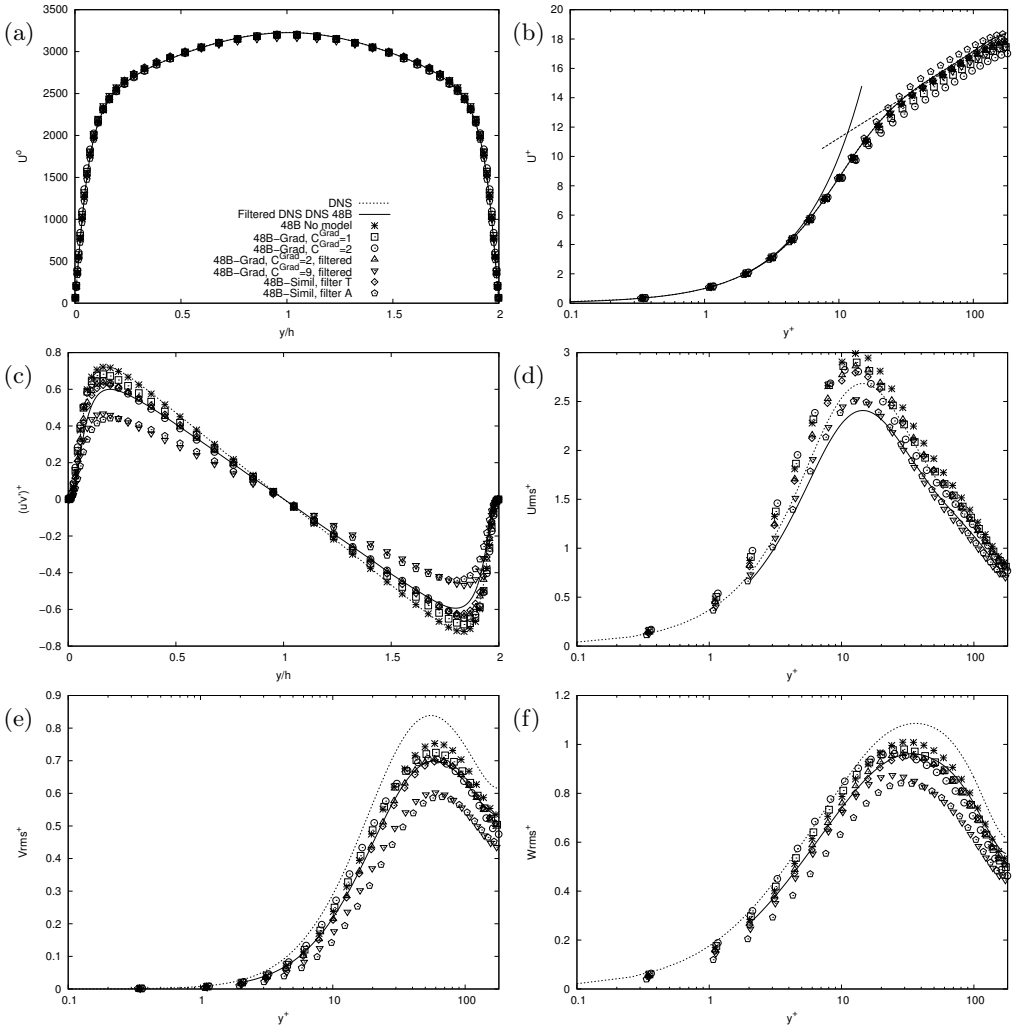

Figure 9 – Comparison of large-eddy simulations with the gradient model using $C^{\text{Grad.}} = 1$ and $C^{\text{Grad.}} = 2$ and the filtered gradient model using $C^{\text{Grad.}} = 2$ and $C^{\text{Grad.}} = 9$ and with the scale-similarity model using filter T and filter A for the profiles of the mean streamwise velocity $\langle U_x \rangle$ (a, b), the covariance of streamwise and wall-normal velocity $\langle u'_x u'_y \rangle$ (c), the standard deviation of streamwise velocity $\sqrt{\langle u'^2_x \rangle}$ (d), wall-normal velocity $\sqrt{\langle u'^2_y \rangle}$ (e) and spanwise velocity $\sqrt{\langle u'^2_z \rangle}$ (f) with the mesh 48B. The filtered gradient model uses the filter A.

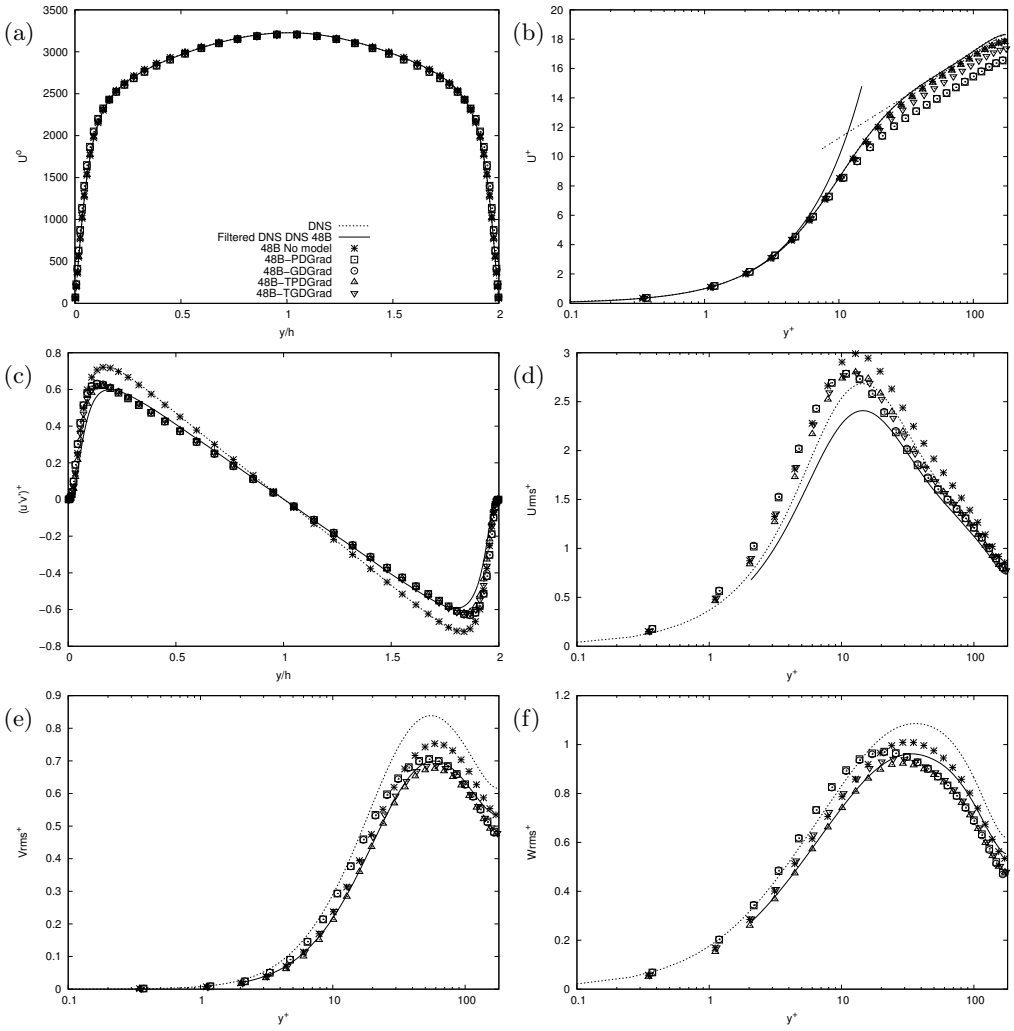

Figure 10 – Comparison of large-eddy simulations with the plane-average, global-average, tensorial plane-average and tensorial global-average dynamic gradient models for the profiles of the mean streamwise velocity $\langle U_x \rangle$ (a, b), the covariance of streamwise and wall-normal velocity $\langle u'_x u'_y \rangle$ (c), the standard deviation of streamwise velocity $\sqrt{\langle u'^2_x \rangle}$ (d), wall-normal velocity $\sqrt{\langle u'^2_y \rangle}$ (e) and spanwise velocity $\sqrt{\langle u'^2_z \rangle}$ (f) with the mesh 48B.

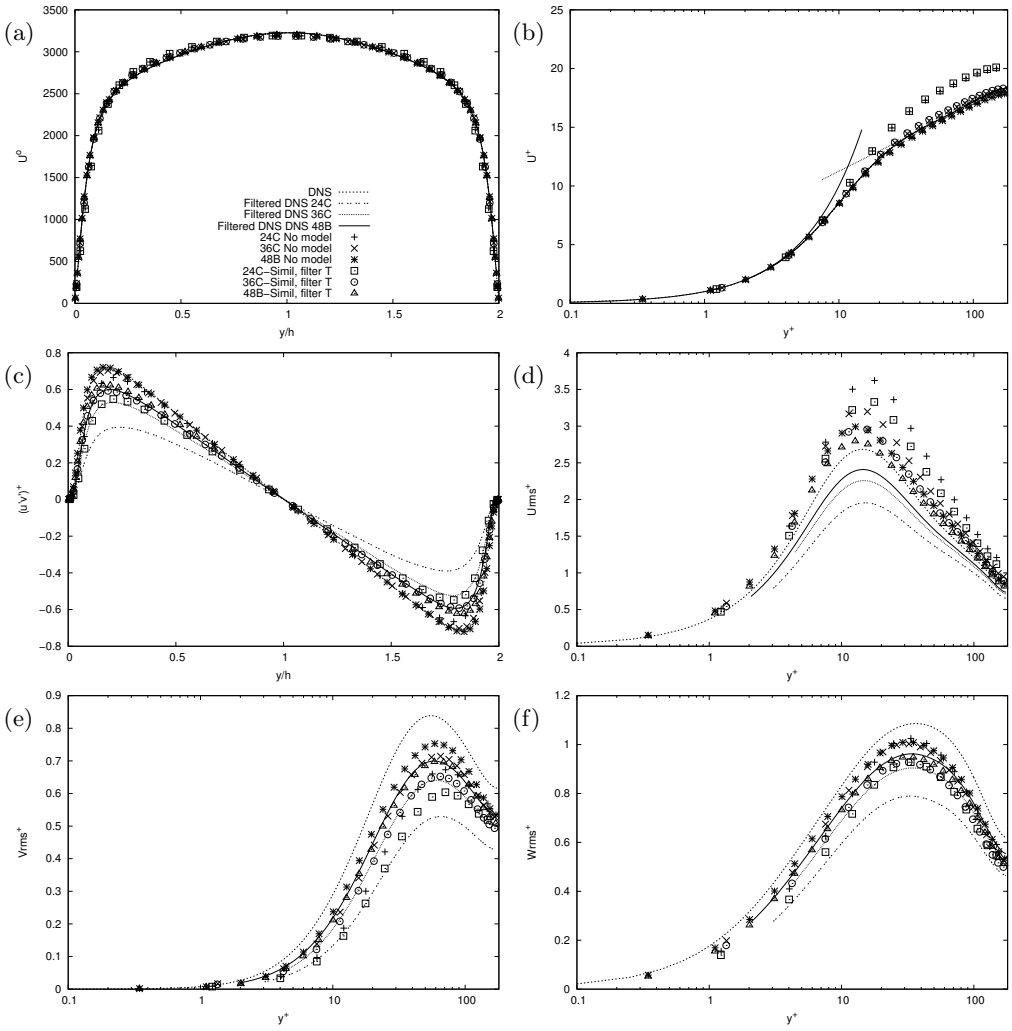

Figure 11 – Comparison of large-eddy simulations with the scale-similarity model using filter T with the meshes 24C, 36C and 48B for the profiles of the mean streamwise velocity $\langle U_x \rangle$ (a, b), the covariance of streamwise and wall-normal velocity $\langle u'_x u'_y \rangle$ (c), the standard deviation of streamwise velocity $\sqrt{\langle u'^2_x \rangle}$ (d), wall-normal velocity $\sqrt{\langle u'^2_y \rangle}$ (e) and spanwise velocity $\sqrt{\langle u'^2_z \rangle}$ (f).

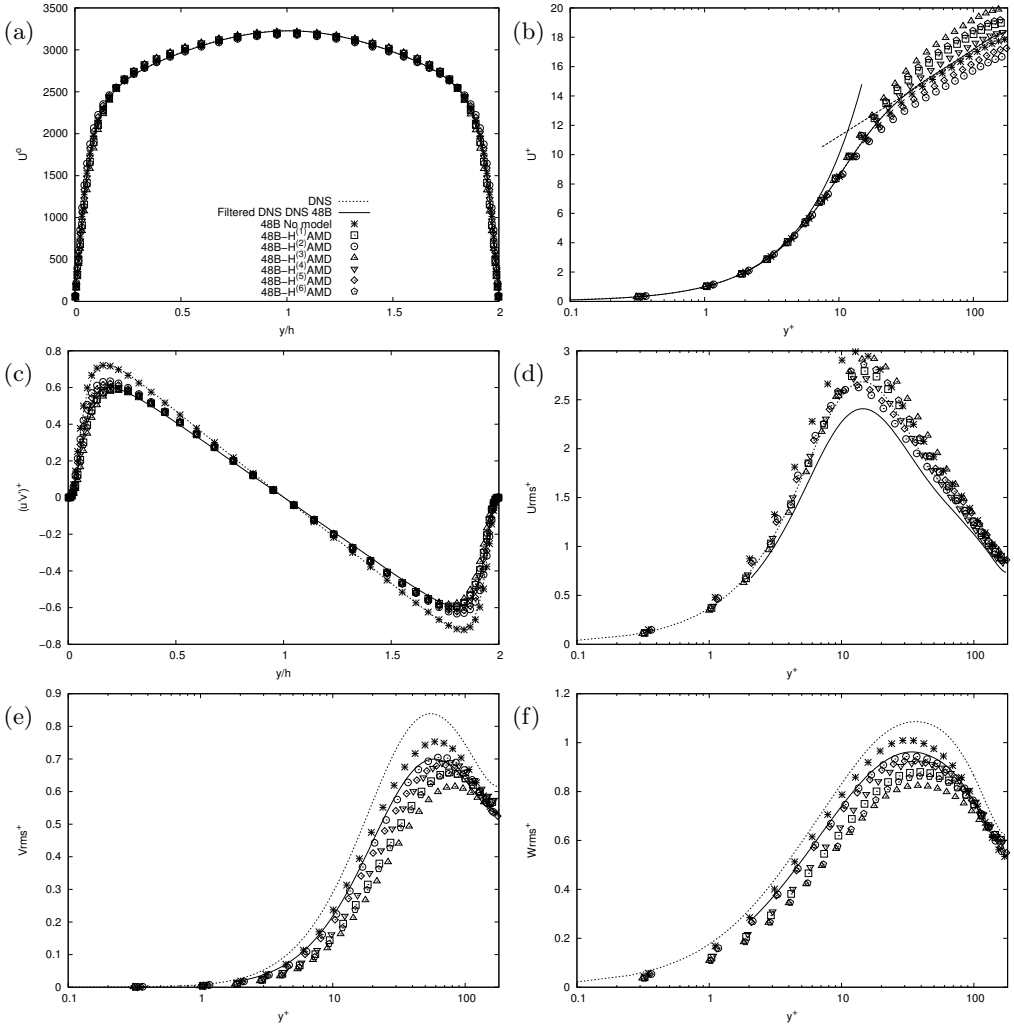

Figure 12 – Comparison of large-eddy simulations with tensorial AMD models for the profiles of the mean streamwise velocity $\langle U_x \rangle$ (a, b), the covariance of streamwise and wall-normal velocity $\langle u'_x u'_y \rangle$ (c), the standard deviation of streamwise velocity $\sqrt{\langle u'^2_x \rangle}$ (d), wall-normal velocity $\sqrt{\langle u'^2_y \rangle}$ (e) and spanwise velocity $\sqrt{\langle u'^2_z \rangle}$ (f) with the mesh 48B.

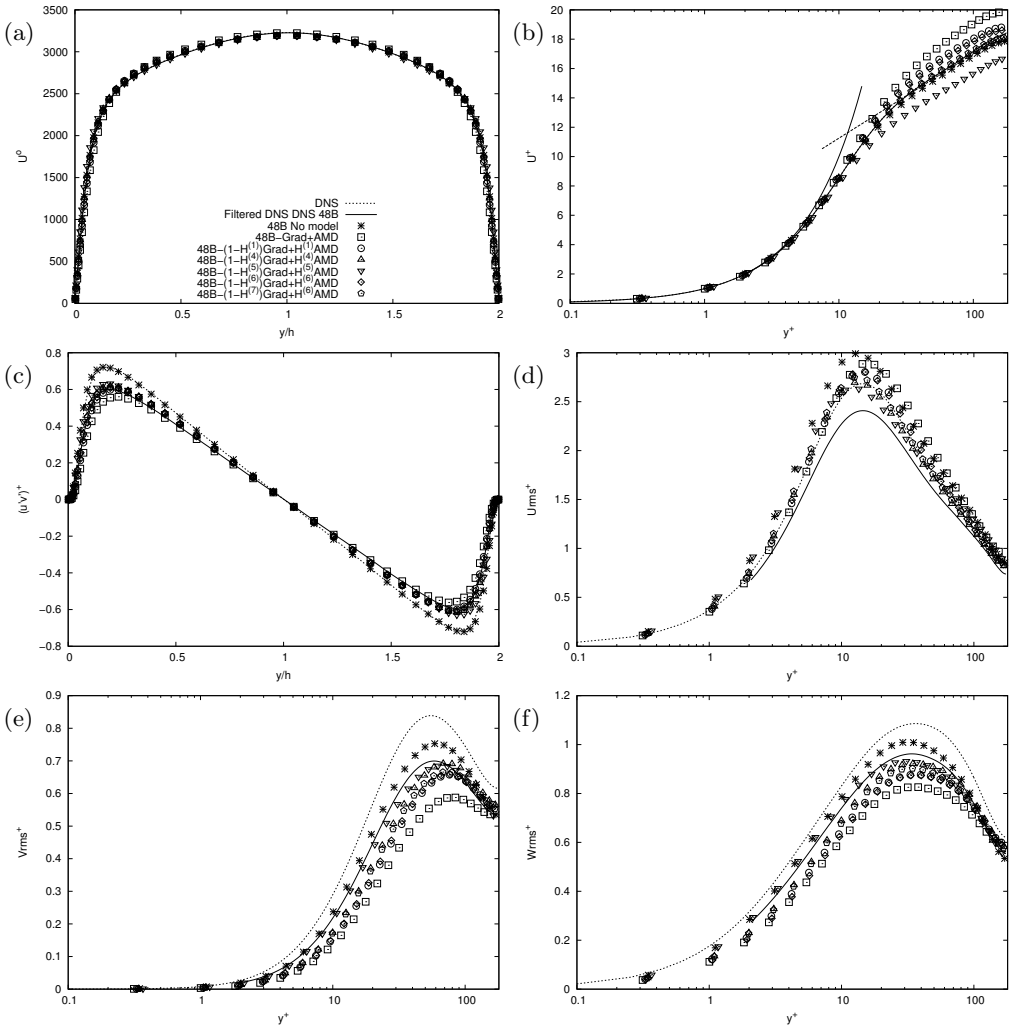

Figure 13 – Comparison of large-eddy simulations with the gradient-AMD mixed model and tensorial gradient-AMD mixed models for the profiles of the mean streamwise velocity $\langle U_x \rangle$ (a, b), the covariance of streamwise and wall-normal velocity $\langle u'_x u'_y \rangle$ (c), the standard deviation of streamwise velocity $\sqrt{\langle u'^2_x \rangle}$ (d), wall-normal velocity $\sqrt{\langle u'^2_y \rangle}$ (e) and spanwise velocity $\sqrt{\langle u'^2_z \rangle}$ (f) with the mesh 48B.

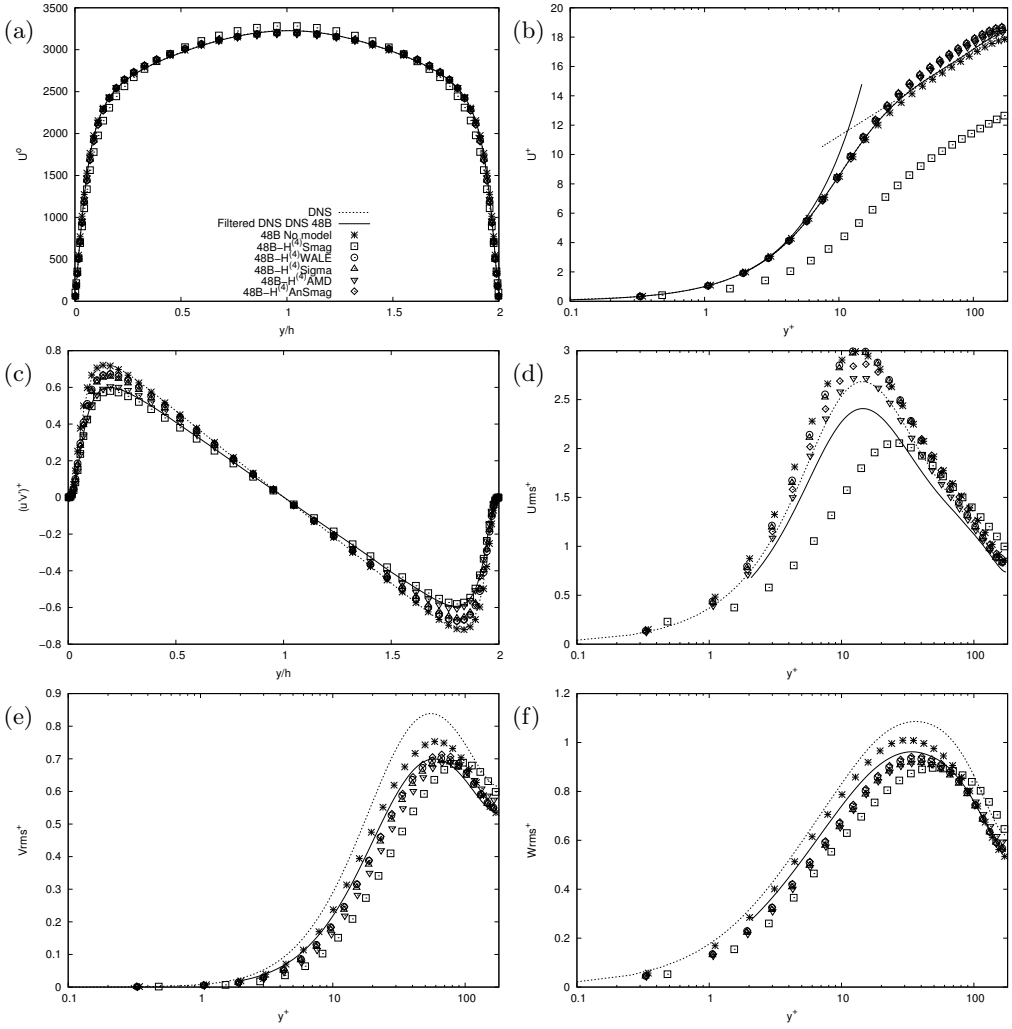

Figure 14 – Comparison of large-eddy simulations with tensorial gradient-Smagorinsky, gradient-WALE, gradient-Sigma, gradient-AMD and gradient-Anisotropic-Smagorinsky mixed models for the profiles of the mean streamwise velocity $\langle U_x \rangle$ (a, b), the covariance of streamwise and wall-normal velocity $\langle u'_x u'_y \rangle$ (c), the standard deviation of streamwise velocity $\sqrt{\langle u'^2_x \rangle}$ (d), wall-normal velocity $\sqrt{\langle u'^2_y \rangle}$ (e) and spanwise velocity $\sqrt{\langle u'^2_z \rangle}$ (f) with the mesh 48B.

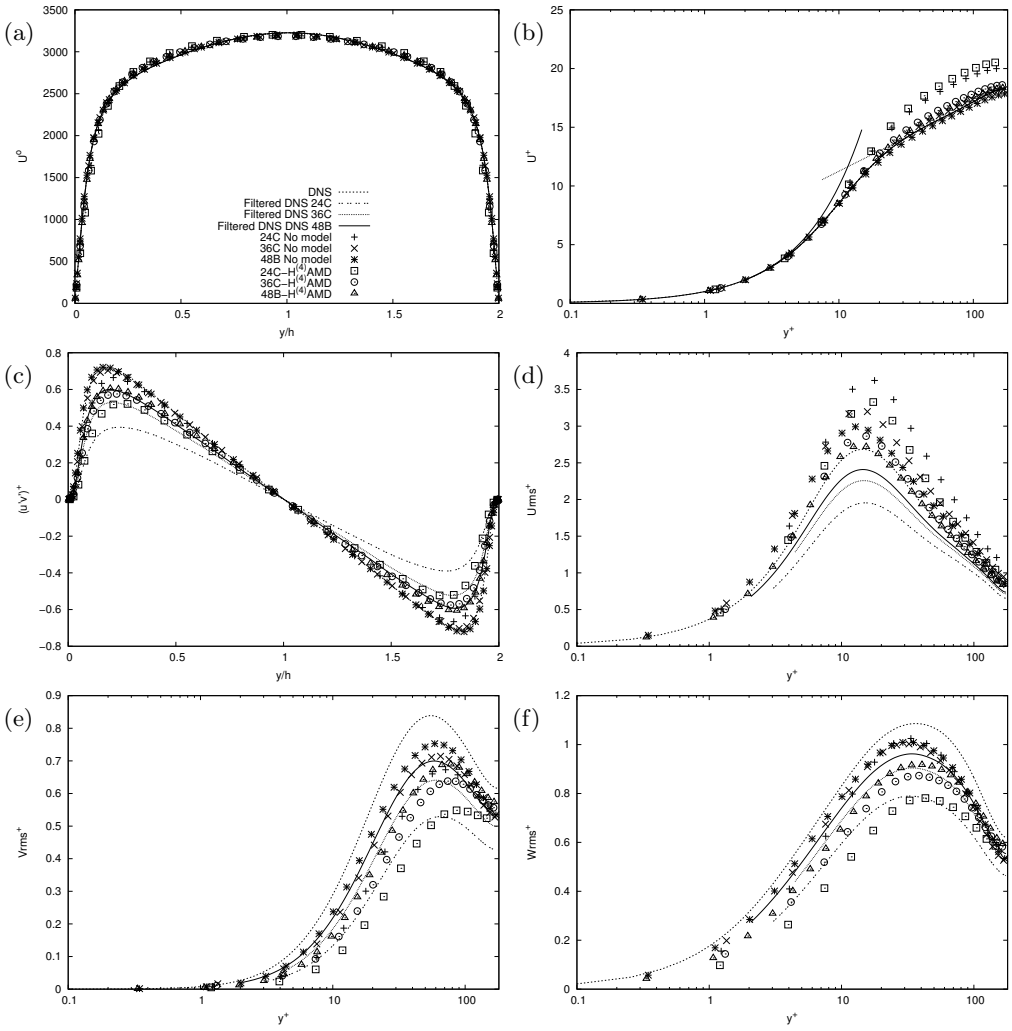

Figure 15 – Comparison of large-eddy simulations with the tensorial gradient-AMD mixed model based on the $H^{(4)}$ (equation 18) tensor with the meshes 24C, 36C and 48B for the profiles of the mean streamwise velocity $\langle U_x \rangle$ (a, b), the covariance of streamwise and wall-normal velocity $\langle u'_x u'_y \rangle$ (c), the standard deviation of streamwise velocity $\sqrt{\langle u'^2_x \rangle}$ (d), wall-normal velocity $\sqrt{\langle u'^2_y \rangle}$ (e) and spanwise velocity $\sqrt{\langle u'^2_z \rangle}$ (f).

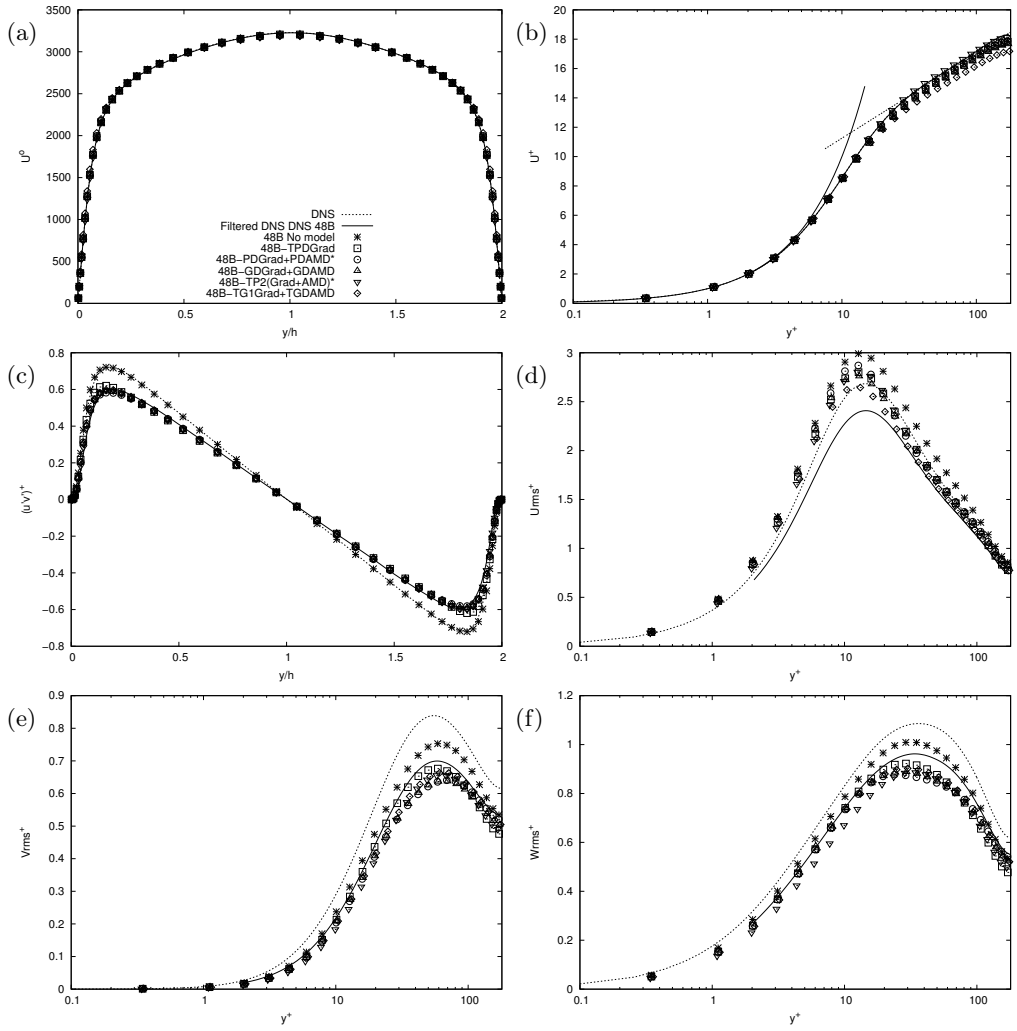

Figure 16 – Comparison of large-eddy simulations with dynamic gradient-AMD mixed models for the profiles of the mean streamwise velocity $\langle U_x \rangle$ (a, b), the covariance of streamwise and wall-normal velocity $\langle u'_x u'_y \rangle$ (c), the standard deviation of streamwise velocity $\sqrt{\langle u'^2_x \rangle}$ (d), wall-normal velocity $\sqrt{\langle u'^2_y \rangle}$ (e) and spanwise velocity $\sqrt{\langle u'^2_z \rangle}$ (f) with the mesh 48B. An asterisk (*) indicates the clipping of the AMD-related part.